

**TUNABLE FOLDED-SLOT ANTENNA WITH THIN FILM
FERROELECTRIC MATERIAL**

By

Amada M. Castro Vilaró

A thesis submitted in partial fulfillment of the
requirements for the degree of

MASTER of SCIENCES

in

Electrical Engineering

UNIVERSITY OF PUERTO RICO
MAYAGÜEZ CAMPUS
2003

Approved by:

José Colom, PhD.
Member, Graduate Committee

Date

Félix Fernández, PhD.
Member, Graduate Committee

Date

Rafael Rodríguez, PhD.
President, Graduate Committee

Date

Lionel Orama, PhD.
Graduate Studies Representative

Date

José L. Cruz, PhD.
Chairperson of the Department

Date

Abstract

In this work, the modeled performance of gold (Au)/ $\text{Ba}_{0.60}\text{Sr}_{0.40}\text{TiO}_3$ (BSTO) ferroelectric/ magnesium oxide (MgO) two-layered tunable coplanar waveguide (CPW) fed folded-slot antenna (FSA) is presented. BSTO materials have electric field dependent dielectric properties. Upon application of electric fields the dielectric constant can be tuned over a wide frequency range. The Finite Difference Time Domain (FDTD) method is applied to analyze the output responses. The return loss, input impedance and elevation patterns of the CPW-fed FSA design are included. The designed antenna structure is operational at Ka-band, matched at 50 ohms with minimum reflections and tunable bandwidth of 7.10 GHz for 23.33% around 30.47 GHz. A total frequency shift of 4 GHz and input resistance shift of 28.54 ohms are obtained. The gain is approximately 2.98 dBi. This thesis research demonstrates another advantageous application for ferroelectric thin-films for enhancing the performance of a CPW-fed FSA designed for Ka-band frequencies.

Resumen

En este trabajo se presenta el desempeño de una antena de ranura plegada de dos capas alimentada por guía de onda coplanar. Su estructura se compone del plano de tierra (Au), una capa de material ferroeléctrico, $\text{Ba}_{0.60}\text{Sr}_{0.40}\text{TiO}_3$ (BSTO) y de una capa de sustrato, Oxido de Magnesio (MgO). La sintonización de dicha antena se debe a las propiedades dieléctricas del BSTO. Al aplicarle un campo eléctrico a este material su constante dieléctrica se puede sintonizar en un rango de frecuencia amplio. El método de diferencias finitas en el dominio del tiempo se aplica para el análisis de las respuestas de salida. Las reflexiones, impedancia de entrada y el patrón de elevación de la antena están incluidas. La antena presentada opera en la banda Ka, está pareada a 50 ohmios, tiene reflexiones bajas y la sintonización de su ancho de banda es de 7.10 GHz para 23.33% alrededor de 30.47 GHz. Dicha antena presenta un desplazamiento total en frecuencia de 4 GHz y en impedancia de entrada de 28.54 ohmios. Su ganancia es de aproximadamente de 2.98 dBi. Esta tesis de investigación demuestra otra aplicación ventajosa para materiales ferroeléctricos para realzar el desempeño de una antena de ranura doblada alimentada por guía de onda coplanar diseñada para frecuencias de la banda Ka.

Dedication

It's an honor for me to dedicate this thesis to my advisor Dr. Rafael Rodríguez. His enthusiasm and uniqueness in teaching his electromagnetic course motivated me to join his research group. His dedication and faith in me truly made a difference in my life.

The Lord blessed me with a wonderful advisor, no doubt there will be extra stars in his crown when he gets to heaven for not only putting up with me, but also for his painstaking review of several drafts of this thesis. I thank him for everything and I hope I made him proud.

Acknowledgements

In preparing this work, I have been able to profit from the advice and suggestions kindly offered by many talented individuals. It is my pleasure to thank them. First and foremost, I would like to acknowledge my most sincere gratitude to my committee professors; Dr. Rafael A. Rodriguez, Dr. José Colom, Dr. Félix Fernández and Dr. Lionel Orama. I would like to express my grateful thanks to Dr. Rafael A. Rodriguez for his critical review and the many constructive suggestions for improving this thesis research. I thank him for catching those pesky grammatical errors. I am most appreciative of Dr. José Colom and Dr. Lionel Orama for their helpful comments and suggestions in reading my thesis. I specially would like to thank Dr. Félix Fernández for his excellent support and for providing the ferroelectric materials and facilities for their measurements.

It is also my pleasure to gratefully acknowledge the kind support of Dr. Félix Miranda and Dr. Frederick Van Keuls from NASA Glenn Research Center for their advice and expertise on ferroelectric materials. Special thanks go to my friends Néstor López and Ileana Carrasquillo from the Radiation Laboratory for answering my questions with the gift of their experience.

Finally, I wish to express my deepest appreciation to my parents, for their love and faith in me throughout my life and to Edgar Seín, for his patience and sacrifices during this often difficult effort.

Table of Contents

List of Tables.....	viii
List of Figures.....	ix
Chapter 1. Introduction.....	1
1.1 Background.....	1
1.2 Objectives.....	3
1.3 Thesis Organization.....	4
Chapter 2. Literature Review.....	5
2.1 Microstrip Antenna Technology.....	5
2.2 Feeding Techniques.....	6
2.2.1 CPW-fed Antenna Publications.....	6
2.2.1.1 CPW-fed Patch Antennas.....	7
2.2.1.2 CPW-fed Slot Antennas.....	8
2.2.1.3 CPW-fed Folded-Slot Antennas....	9
2.2.1.4 CPW-fed Array Antennas.....	14
2.3 Dual Frequency Microstrip Antennas.....	18
2.4 Ferroelectric Antennas.....	21
2.4.1 BSTO Publications.....	22
2.5 Simulation Software.....	27
2.6 Chapter Conclusions.....	29
Chapter 3. Methodology.....	30
3.1 Purpose.....	30
3.2 Procedure.....	31
3.3 Simulation Software.....	32
3.3.1 LineCalc Software.....	32
3.3.2 XFDTD Software.....	33

3.3.2.1	FDTD Method.....	33
3.3.3	Design Expert Software.....	35
3.3.3.1	Geometrical Design.....	35
3.3.3.2	Goal-model Design Process.....	36
3.4	Design Dimensions.....	37
3.5	Design of Experiment.....	38
3.6	Prototype Fabrication.....	43
3.6.1	PLD Technique.....	43
3.7	Film Characterization.....	45
3.8	Chapter Conclusions.....	47
Chapter 4.	Results and Discussions.....	48
4.1	Preliminary Dimensions.....	48
4.2	Matching Dimensions.....	52
4.3	Space Step Variation.....	59
4.4	Thin Film Relative Permittivity Variation.....	64
4.5	Design of Experiment.....	68
4.6	Goal-model Development.....	83
4.7	Film Characterization Scan.....	89
Chapter 5.	Conclusions and Recommendations.....	91
5.1	Conclusions.....	91
5.2	Recommendations.....	93
References	94

List of Tables

Table 2.1	Dielectric Substrate Parameters and CPA Geometric Dimensions.....	8
Table 4.1	CPW Feed Dimensions.....	48
Table 4.2	SFSA Preliminary Dimensions.....	49
Table 4.3	AFSA Matching Dimensions.....	57
Table 4.4	AFSA Matching Dimensions at New Space Step...	61
Table 4.5	DoE Input Factors.....	68
Table 4.6	DoE Geometrical Design Combinations.....	68
Table 4.7	Relative Permittivity Coded Values.....	85
Table 4.8	Validation Design Dimensions.....	86
Table 4.9	Validation Design Combinations.....	86
Table 4.10	Output Response Comparison at $\epsilon_{xf}=400$	87
Table 4.11	Output Response Comparison at $\epsilon_{xf}=800$	87
Table 4.12	Output Response Comparison at $\epsilon_{xf}=1200$	87

List of Figures

Figure 2.1	Configuration of CPW-fed CPA.....	7
Figure 2.2	Geometries of various slot antenna configurations.....	9
Figure 2.3	Folded slot antenna.....	10
Figure 2.4	Impedance scaling by multiple-slots.....	12
Figure 2.5	Schematic of microwave FSA with parameters..	13
Figure 2.6	Quasi-optical reflection amplifier cell.....	15
Figure 2.7	Circularly polarized slot antenna.....	16
Figure 2.8	Plan view of the folded-slot planar amplifier cell.....	17
Figure 2.9	Measured effective isotropic power gain of the planar amplifier array.....	18
Figure 2.10	CPW-fed antenna controlled by pin diodes....	20
Figure 2.11	Schematic of a single layer tunable BSTO ferroelectric antenna.....	22
Figure 2.12	Measured unbiased reflection loss and gain performance.....	23
Figure 2.13	Ferroelectric antenna with superstrate cover	24
Figure 2.14	Multilayered antenna with parasitic radiator	25
Figure 2.15	Schematic of a multilayered direct stacking dual band antenna.....	26
Figure 2.16	Measured unbiased gain performance.....	27
Figure 2.17	Computational domain of CPW-fed FSA.....	28
Figure 3.1	CPW-fed FSA schematic.....	30
Figure 3.2	CPW-fed FSA design parameters.....	31
Figure 3.3	Geometrical representation of DoE input factors.....	39
Figure 3.4	Bull's Eye graphical representation of the output responses.....	41

Figure 3.5	PLD process.....	44
Figure 3.6	Visualization of Bragg's Law.....	46
Figure 4.1	SFSA simulated results with and without the applied ferroelectric material.....	50
Figure 4.2	Top slot width variation.....	52
Figure 4.3	Separation between top and bottom slot width variation.....	53
Figure 4.4	Side slot width variation.....	54
Figure 4.5	Bottom slot width variation.....	55
Figure 4.6	Simulated return loss of the preliminary and matching dimensions.....	57
Figure 4.7	Simulated input impedance of the preliminary and matching dimensions.....	58
Figure 4.8	AFSA simulated results at old and new space steps.....	60
Figure 4.9	Matched AFSA simulated results at old and new space steps.....	62
Figure 4.10	CPW-fed FSA simulated results at varied film relative permittivity.....	65
Figure 4.11	DoE graphical visualization with Bull's Eye representation of the goal responses simulated at the respective input factors.....	70
Figure 4.12	DoE graphical visualization with Bulls Eye representation of the dual resonance behavior simulated at the respective input factors...	72
Figure 4.13	Design 3 simulated results at varied film relative permittivity.....	74
Figure 4.14	Design 12 simulated results at varied film relative permittivity.....	77
Figure 4.15	Optimum designs at film relative permittivity of 80.....	80
Figure 4.16	θ - 2θ scan of the BSTO/MgO sample.....	89

CHAPTER 1

Introduction

1.1 Background

The recent explosion in wireless communications has fueled the interest in tunable devices for microwave and millimeter-wave applications. Next-generation mobile phones and other wireless communication systems must be capable to adapt to and operate in systems with different standards, networks, and operating frequencies. Such systems must provide very large bandwidths to cope with the large number of users and the high data rate service users demand.

In order to achieve higher data transmission rates, larger bandwidths and more efficient use of the available bandwidth is necessary. This need for higher bandwidths and thus higher data transmission rates will push the wireless communications systems to higher frequency bands in the microwave and millimeter-wave regions. Because the frequency spectrum is already crowded at frequencies up to Ku-band (12-18 GHz), it is imperative that low-cost mobile units capable of transmitting and receiving signals at K-band (18-26.5 GHz) and Ka-band (26.5-40 GHz) be developed to make broadband service available to mobile users.

The need for this mixed-traffic, high mobile networks require that special consideration be given to the antennas used. In order for these antennas to be useful it is necessary that they provide large bandwidths and must be small and low profile to be located at the mobile terminals while keeping the terminal size and weight down. At higher microwave frequencies and at the millimeter-wave frequency range, the use of slot antennas is more prevalent. Folded slot antennas are attractive for active devices due to

relatively large bandwidth, fabrication simplicity, and ease integration with devices. In order to reduce the size and improve the performance of the antenna a coplanar waveguide feed technique is applied to the folded slot antenna. Because of the need for low capacitance and low loss for tunable devices, there is substantial interest in thin-film tunable dielectric materials. Devices with thin-film material have configurations that are compatible with planar microwave circuits, and thus are preferred to bulk devices.

The concept of exploiting the voltage-dependent dielectric constant of ferroelectric and tunable dielectric materials such as $\text{Ba}_x\text{Sr}_{1-x}\text{TiO}_3$ (BSTO) for microwave tuning applications are being developed for use in next-generation, broadband wireless communication systems. At millimeter-wave frequencies, ferrites become more attractive because the device size decreases with increasing frequency and thus the drive powers for the tuning circuitry also decreases. Some of the characteristics that make tunable dielectric materials attractive for wireless communications are reasonably high Q at microwave and millimeter-wave frequencies, planar structures, which make them compatible with microstrip and finline configurations, low dc power consumption, high RF power-handling capabilities at Ka-band, and low manufacturing cost. These characteristics can be advantageous in a wide variety of devices. Devices that use these materials as the control elements may potentially play a major role in the evolution of broadband wireless systems.

1.2 Objectives

This thesis has the importance to investigate the use of ferroelectric materials in the design and fabrication of tunable folded-slot antennas. The main objective of this investigative work is to design and characterize a tunable folded-slot antenna with thin film ferroelectric material. Explore the effects of the antenna layout and the application of thin ferroelectric film on the matching resonant frequency (f_r), reflections (S_{11}), bandwidth (BW), input impedance (Z_{in}) and gain (G). Also, throughout this research optimum dimensions for the antenna will be obtain in order to have better performance.

It is desirable that the antenna be tunable, operation at Ka-band, with minimum reflections ($S_{11} < -20$ dB), wide bandwidth ($BW \geq 3$ GHz), and impedance matching at 50 ohms with gain greater than 2 dBi. The antenna configuration consists of two layers: one is the substrate and on top of this, there is the dielectric (ferroelectric material) and on the ground plane, the folded-slot antenna fed by coplanar waveguide transmission line. To the knowledge of the authors, tunable slot antennas using thin film ferroelectric have not been reported in literature.

1.3 Thesis Organization

Chapter 2 of this thesis presents a literature review of the most commonly used antenna structures and ferroelectric materials at microwave frequencies. The results of these previous investigative works will be introduced, as well as the antenna and ferroelectric characteristics. In Chapter 3, the materials and methodology used to accomplish this thesis research are described. The proposed antenna structures, design process, simulation software and results (f_r , S_{11} , BW , Z_{in} and G) will be presented. The development of a design of experiment to obtain a model of the antenna structure is also included. Chapter 4 consists of presenting, analyzing and explaining the obtained results. Chapter 5 consists of presenting a summary, achievements and conclusions concerning this thesis and recommendations for further designs.

CHAPTER 2

Literature Revision

2.1 Microstrip Antenna Technology

Microstrip antenna technology has been the most rapidly developing research topic in the antenna field, because of the huge demand in the markets of personal and satellite communications, wireless local networks and intelligent vehicle systems. These devices are well known for their highly desirable physical characteristics such as low profile, light weight, low cost and ruggedness and they are also well suited to integration with integrated circuits and MMICs.

At microwave frequencies, the most commonly used antenna structure is the rectangular microstrip patch, since it is well known and easy to fabricate. The rectangular patch has the advantage of being planar and relatively small, depending on the substrate used. In comparison to traditional antenna elements, however, the electrical performance of the basic microstrip antenna suffers from a number of serious drawbacks, e.g. narrow bandwidth; high feed network losses, poor cross polarization, and low power handling capacity.

At higher microwave frequencies and at the millimeter-wave frequency range, the use of slot antennas is more prevalent. Slots also suffer from limited bandwidth problem and few bandwidth enhancement techniques for slots can be found in the literature. Folded slot antennas (FSA), on the other hand, are attractive for active devices due to relatively large bandwidth, fabrication simplicity, and ease integration with devices. Currently, there is little design information for these antennas, especially on thin

substrates. Relative to the simple slot antenna, the folded-slot is approximately the same physical size at the first useful resonance and provides input impedance that is four times lower. The folded-slot can provide significantly wider bandwidths, in the order of 10%, than patch antennas. Folded slots can be implemented without the need for matching networks when using the impedance matching technique (IMT) presented in [1]. This IMT varies the width of the FSA in order to reduce its input impedance to 50 ohms without varying the length of the antenna.

2.2 Feeding Techniques

The popularity of the coplanar waveguide (CPW) transmission line has increased significantly in recent years. CPW transmission lines have lower radiation loss and less dispersion than microstrip lines. Furthermore, the characteristic impedance and phase velocity of CPW are less dependent on the substrate height and more dependent on the dimensions in the plane of the conducting surface. The main advantage of CPW is easier integration with solid state devices by eliminating the need for via holes.

2.2.1 CPW-fed Antenna Publications

Many studies have been made on antennas fed by CPW transmission line such as patches [2], slots [3] and folded-slots [1, 4, 5]. CPW-fed antennas have been used as the radiating element in quasi-optical, circularly polarized and planar arrays [6, 7, 8]. The characteristics for CPW-fed antennas have been described in [1, 4]. The following sections present some published results.

2.2.1.1 CPW-fed Patch Antennas

Coplanar patch antennas (CPA) have been used for operation at microwave frequency [2]. This antenna consisted of a patch surrounded by closely spaced ground conductor. The background conductor provides unidirectional radiation pattern and easy mounting, packing and integration with other microwave circuit devices. The CPA configuration is shown in Figure 2.1 where as its design dimensions are shown in Table 2.1. The antenna looked very similar to the loop antenna but it was discovered that the antenna behaved more like a microstrip antenna because its resonant frequency was determined by the patch length (L) and its impedance matching by adjusting its width (W).

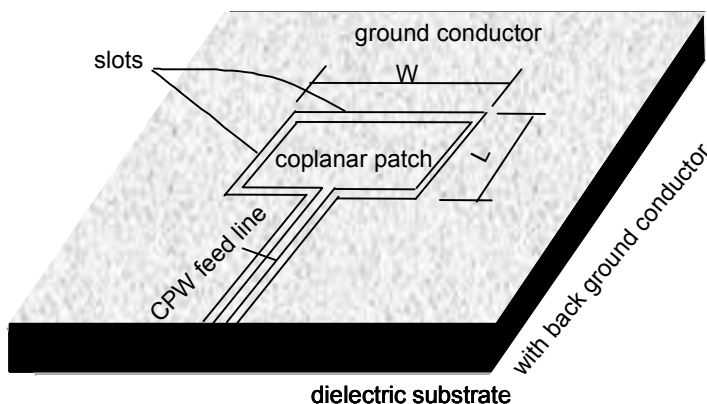
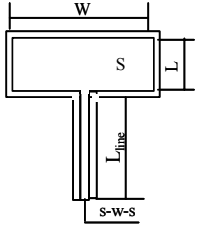


Figure 2.1. Configuration of CPW-fed CPA. (Taken from [2]).

Table 2.1
Dielectric Substrate Parameters and CPA Geometric Dimensions
(Taken from [2])

Dielectric substrate (DIECLAD880, ARLON)	ϵ_r	$\tan \delta$ (@ 10GHz)	Thickness of substrate	Metal film	
	2.17	0.00085	0.508	Cu 18 μ m	
Coplanar Waveguide (CPW)	s-w-s	L_{line}	Unit: mm		
	1.0-1.6-1.0	10			
Coplanar patch antenna	L	W	S		
	0.55	31.0	1.0		

The CPA was operational at X-band (10 GHz) on a conductor backed dielectric with relative dielectric constant of 2.17. There was a good agreement between the measured and simulated return loss results. The antenna had a bandwidth of 3.4% at -10 dB return loss. Measured cross polarization was under -23 dB in E-plane while there was a maximum value -17 dB in H-plane. The CPA had a gain 7.8 dBi which was 1.1 dB lower than the simulated gain of 8.9 dBi.

2.2.1.2 CPW-fed Slot Antennas

Various slot antenna configurations have been investigated and reported in literature. Some of these have been center-fed slots and coplanar waveguide fed slots [3]. These slots were fed by an impressed magnetic field by MoM, which were used to describe by interference the resonant mode on the finite slot [3]. The center-fed and CPW-fed slot structures were characterized by appropriate entire domain basis functions with respect to the center of the finite slot to describe the magnetic currents. The configurations are shown below and its insets show the detail of the feed.

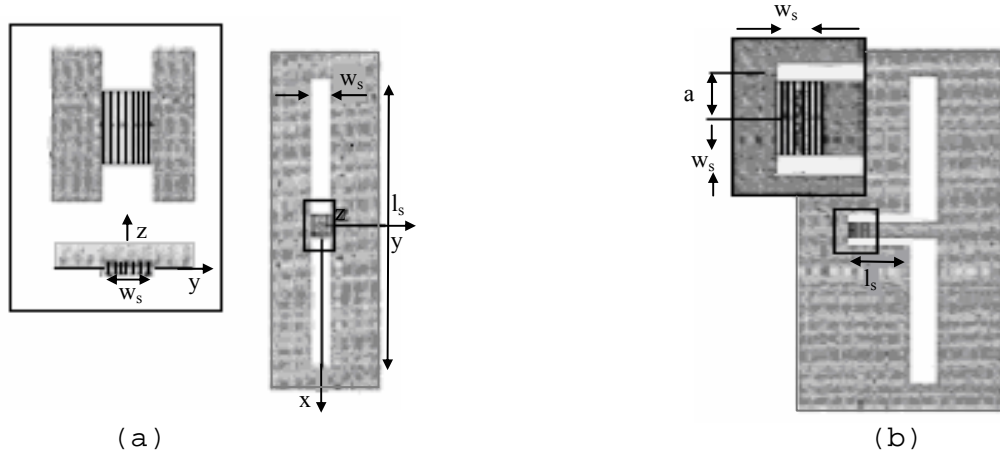


Figure 2.2. Geometries of various slot antenna configurations. a) Center-fed slot. b) CPW-fed slot. (Taken from [3]).

The structures were implemented to operate at 500 GHz with a slot length (l_s) and width (w_s) of 210 and 10 μm respectively. For both cases the dielectric constants were $\epsilon_{r1} = 11.7$ (silicon) and $\epsilon_{r2} = 1$. Through simulation it was proved that the CPW-fed slot antenna represented the practical realization of the center-fed slot when assuming that the inner conductor of the CPW had the same width of the center-fed current width.

2.2.1.3 CPW-fed Folded-Slot Antennas

Many studies have been made on folded-slot antennas (FSA) fed by CPW transmission line. There have been publications introducing the characteristics of FSA [4], describing the problems encountered in the analysis of such structure [5], as well as impedance matching techniques [1].

In [4] the behavior of a FSA was compared with a center fed slot antenna. A schematic of the FSA and the self-impedance for the simple and folded slot antennas are shown

in Figure 2.3. The FSA dimensions were $W_{a1}/W_{a2}/S_a/L_a = 0.10/0.20/0.10/10$ and its feed dimensions were $W_f/S_f = 0.10/0.40$, all dimensions in mm. The dielectric was silicon with $\epsilon_r = 11.7$.

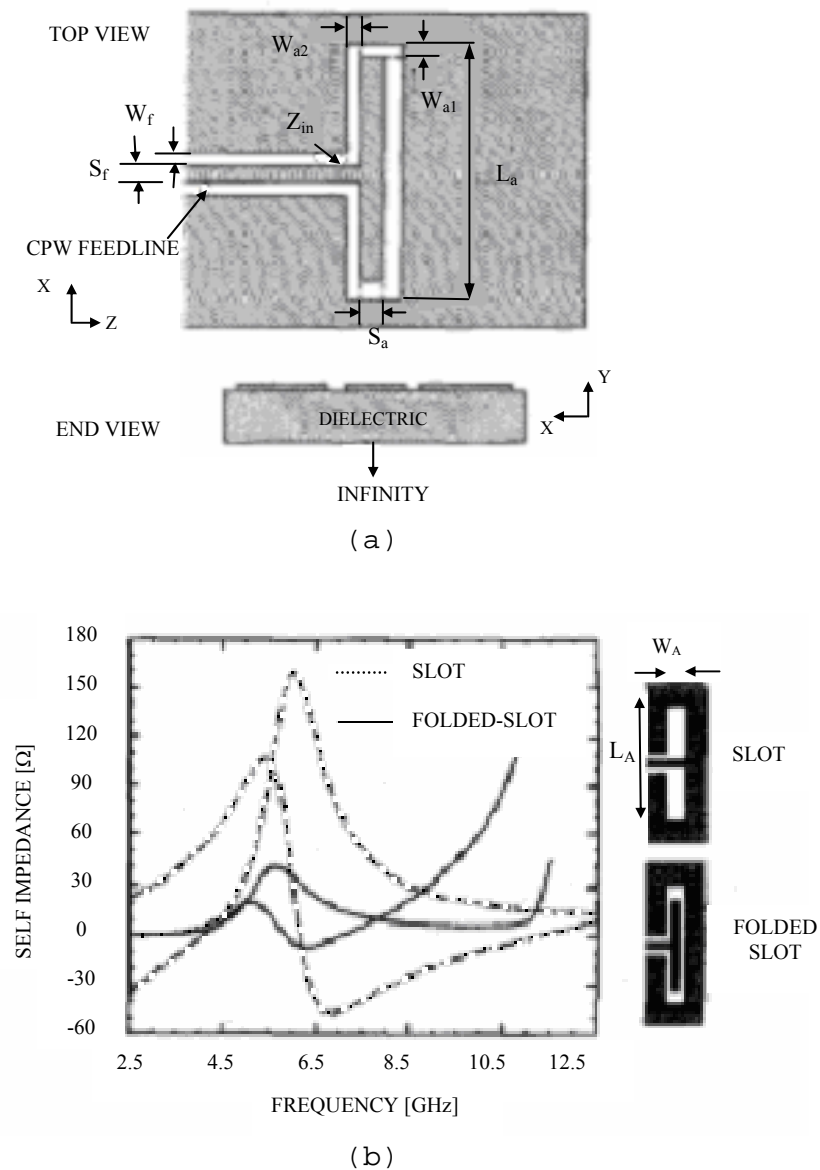
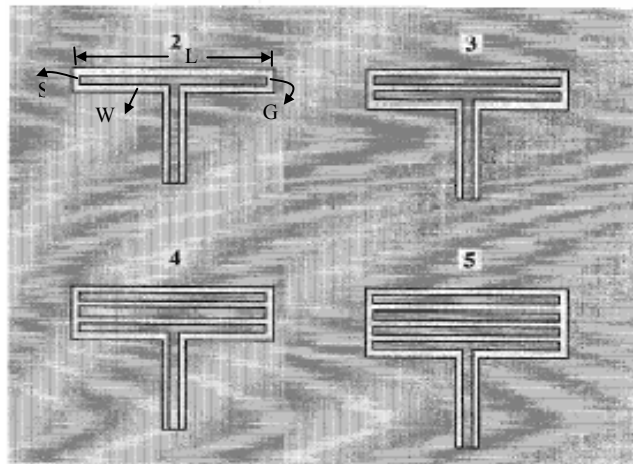


Figure 2.3. Folded slot antenna (a) Schematic diagram. (b) Calculated self-impedance for a FSA and comparable slot antenna. (Taken from [4]).

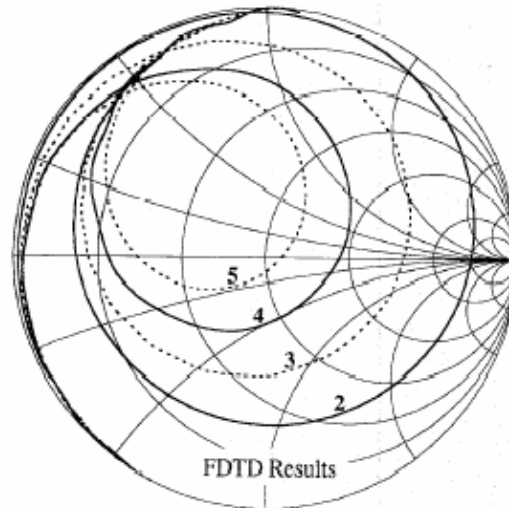
Relative to the slot antenna, the FSA was approximately the same physical size at the first useful resonance and its peak in $Re(Z_{self})$ provided input impedance four times lower. The self-impedance of each antenna at its respective second resonance however was 16 ohms. As presented, the FSA in comparison with the slot antenna is suitable for millimeter-wave applications.

In [5] a FSA structure was measured and simulated at 10 GHz on a high dielectric constant ($\epsilon_r = 9.8$) Alumina substrate with thickness of 0.635 mm. The slot dimensions were $L = 7.2$ mm, $W = S = G = 0.3$ mm. The FSA was studied in order to understand the influence of antenna layout and substrate parameters on the input impedance and bandwidth. A simple transmission line model for the folded slot suggested, and simulations confirmed, that the total slot length around the periphery determined the resonant frequency. It was also demonstrated that an increase in the substrate thickness caused the resonant frequency to decrease. On the other hand, the input impedance was an increasing function of thickness. In addition, the width of the slots had a marked influence on the antenna bandwidth. As this width increased so did the antenna bandwidth.

A method for controlling the impedance over a wide range through multiple slots was also presented in [5]. Since the impedance was an increasing function of thickness for the range $h/L < 0.4$, the required number of slots to achieve the desired impedance will depend critically on these parameters. The following figures illustrate the impedance scaling with the number of slots.



(a)



(b)

Figure 2.4. Impedance scaling by multiple-slots. (a) Antenna layouts. (b) Simulated results. (Taken from [5]).

The input impedance of the folded-slot (2 slots) antenna was approximately 118 ohms; where as 5 slots produced approximately an impedance of 50 ohms. Therefore, including additional parasitic slots was found to provide an excellent means for adjusting the input impedance over a wide range. The limitations in this technique were that the

slots must be situated close to the original slot; there is a limit to the number of slots that can be added in order to maintain the currents in each slot of equal magnitude and in phase.

A new impedance matching technique (IMT) for FSA was presented in [1] in order to improve the limitations of the technique presented in [5]. In the previous publication the slot widths were equal; in this work, the top slot width (W_{a3}) was increased to control the antenna input impedance. The main advantage of this technique over the multiple-slot technique is that the antenna input impedance can be matched to any desired load and that the antennas are simpler to fabricate. Figure 2.5 presents the proposed FSA schematic operational at 3 GHz. This antenna was simulated with various substrates. The substrates tested had relative permittivity (ϵ_r) of 2.33, 6.15 and 10.2, each with thickness (h) of 0.64, 1.30 and 1.90 mm.

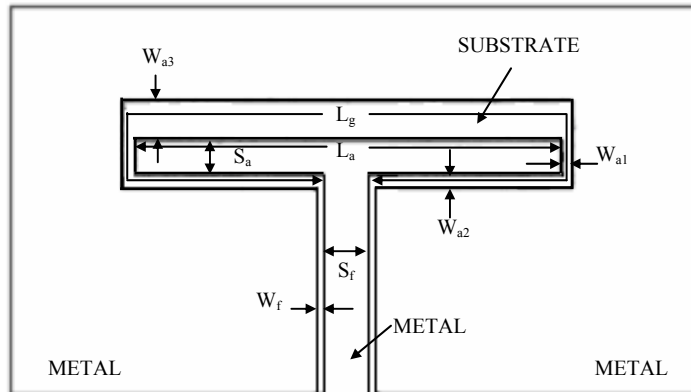


Figure 2.5. Schematic of microwave FSA with parameters. (Taken from [1]).

It was noticed from simulation that the input impedance followed an exponential model with respect to the increment in W_{a3} and that substrates with higher relative permittivity

needed a wider Wa_3 dimension to achieve lower impedance. The FSA with dimensions $La = 15.32$ mm, $Wa_1 = Wa_2 = Sa = Wf = 0.25$ mm, $Sf = 0.606$ mm and substrate with $\epsilon_r = 2.33$ and $h = 1.3$ mm showed that an increase in Wa_3 from 0.25 to 1.1 mm was able to reduce the input impedance from 128.05 to 50.7 ohms. This was an increase from 0.58% to 2.56% with respect to the dimension La .

This structure was also matched through the multiple-slot technique. Four slots were needed to obtain input impedance of 54.5 ohms, resulting in an increase from 2.71% to 8.13% with respect to La . The proposed impedance matching technique was simpler since its performance depended on increasing just one parameter, and from modifying this one parameter exact values for the input impedance were obtained.

2.2.1.4 CPW-fed Array Antennas

Solid-state power combining in free space offers an attractive alternative to vacuum-tube sources for high power millimeter wave applications. In [6] a quasi-optical amplifier cell suitable for power combining arrays was presented. Orthogonally polarized patch antennas are coupled to the input and output of a resistive feedback MESFET amplifier. Reflection amplifiers are attractive because they are compact, and the signals do not propagate through the substrate so the backside can be used for waste heat removal, which will be critical in high-power, high-efficiency designs.

The proposed configuration, with blow-up of resistive feedback amplifier and measured power gain in comparison with frequency response of patch antenna are shown in Figures 2.6 and 2.7. The substrate had a dielectric constant of 10.8 and thickness of 0.635 mm. A NE32184A MESFET

amplifier with feedback resistor of 511 ohms and source and load impedance of 125 ohms was used to operate at 4 GHz. A typical patch antenna gain is around 5 dBi; the peak gain of this array was approximately 17 dBi at 4.2 GHz with 1% bandwidth. The resonant patch antennas on a thin substrate with high dielectric constants limited the bandwidth of this amplifier.

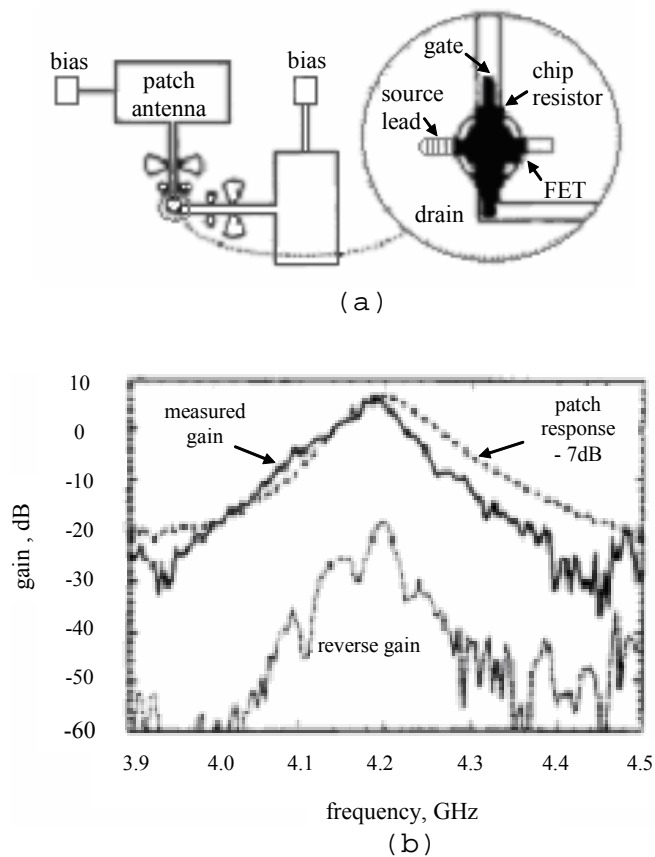


Figure 2.6. Quasi-optical amplifier cell. (a) Plan view of amplifier circuit. (b) Measured forward and reverse power gain of amplifier cell. (Taken from [6]).

A linear array of a circular polarized slot loop antenna fed by CPW was investigated in [7]. The advantages of this antenna are simple structure and easy forming an array without complex feed line. Figure 2.7 presents the

circularly polarized antenna array and antenna element. The array was composed of three pairs of the antenna element producing the circularly polarized wave. The polarization of the element can be switched by changing the location of the feed point. It was shown that the part a1-b1 serves as a slot line and the part b1-c1 acts as a slot antenna. The phase difference between A and B is almost 90° . This distribution met the condition of producing circularly polarized wave. The measured gain was about 12 dBi and this showed that the efficiency of this antenna is very high.

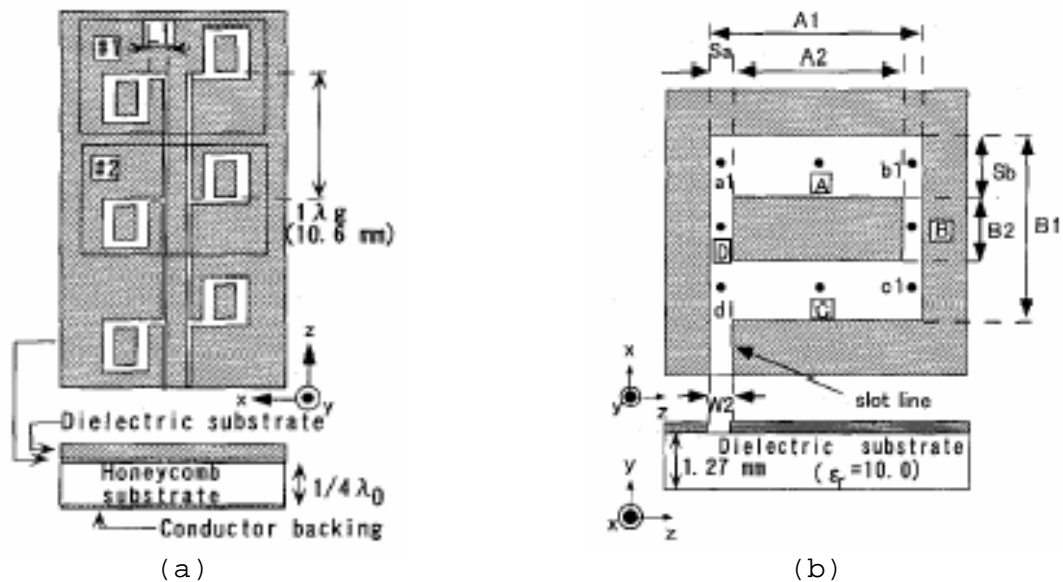


Figure 2.7. Circularly polarized slot antenna. (a) Antenna array fed by CPW. (b) Antenna element fed by slot line. (Taken from [7]).

In [8] a broadband planar amplifier array and a single cell using orthogonally polarized CPW-fed folded-slot antennas coupled to a resistive feedback single-stage MESFET amplifier was reported. The use of folded slots gave an order of magnitude improvement in bandwidth over a previously reported amplifier based on patch antennas [6]

and can be used for either transmission or reflection amplification. The amplifier and substrate design parameters were the same as in [6]. The dimensions for the FSA were $L = 18$ mm, $W = 7$ mm and a gap width of 1 mm. Its configuration and measured results are shown below. The peak effective isotropic power gain in the transmission mode is 11 dBi at 4.3 GHz with 10% bandwidth for the single cell, a factor of ten improvement in bandwidth over a similar cell using patch antennas, and 32 dBi at 4.24 GHz with 8% bandwidth for the array.

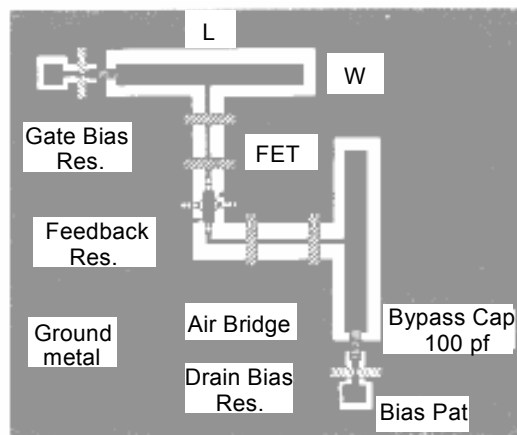


Figure 2.8. Plan view of the folded-slot planar amplifier cell. (Taken from [8]).

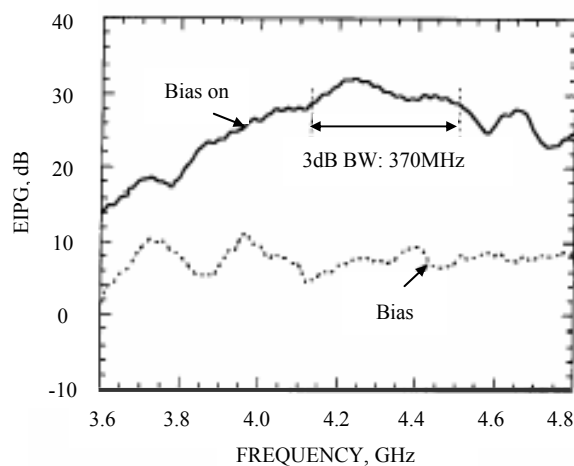


Figure 2.9. Measured effective isotropic power gain of the planar amplifier array. (Taken from [8]).

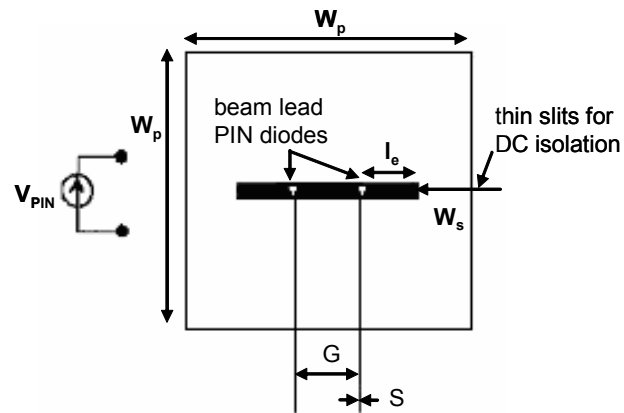
2.3 Dual Frequency Microstrip Antennas

Dual frequency microstrip multi-functional antennas generally have two types of applications in the telecommunications area: applications in which two types of standards are combined such as personal handsets combining GSM and DCS1800 modes in Europe, and applications in which multi frequencies are used for emission and reception such as personal satellite communications and cellular network systems.

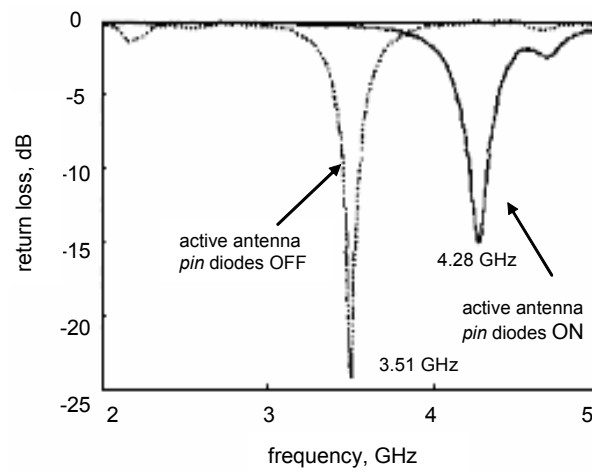
In microstrip antennas, tuning is achieved via variations in the antenna physical structure. Methods for controlling the resonant frequency by varactors and pin diodes have been proposed in [9]. The method with varactors requires a large and continuous range of bias voltages, where as the pin diode method can be sufficient if dual narrow bandwidths are desired with a couple of voltages only. The pin diode method presented in [9] was used to

obtain a dual-band operation of a capacitive coupled patch antenna fed by CPW. The originality of this work consisted in altering the electrical length of the excitation slot with pin diodes instead of the electrical dimensions of the radiating element, which greatly simplifies the biasing circuitry. In this method, when the diodes were in the ON state, they behaved as equivalent short circuits reducing the length of the slot. When the diodes were in the OFF state, the length of the slot remained unchanged. As a result, different resonant frequencies were expected for each diode state.

The geometry of the CPW-fed antenna consisted of thin slits (width = 100 μm) which were used for DC isolation and were covered by metal-insulator-metal capacitors. A patch with width $W_p = 20$ mm, slot with width (W_s) and length (l_e) of 0.5 and 18 mm and CPW fed dimensions of $S = 0.2$ mm and $G = 4.4$ mm. The substrate had a relative permittivity of 2.2 and thickness of 2.3 mm. It was observed through measurement that at the ON state the active antenna resonated at 4.28 GHz and at the OFF state it resonated at 3.51 GHz.



(a)



(b)

Figure 2.10. CPW-fed antenna controlled by pin diodes. (a) Schematic diagram. (b) Measured return loss of antenna including pin diodes for both diode states. (Taken from [9]).

2.4 Ferroelectric Antennas

Voltage-tunable materials are technologically important for frequency-agile microwave applications. The ability to electronically tune the frequency of operation of such devices, by changing the material permittivity under an applied electric field, will enable many high-performance microwave applications. Tunable Barium Strontium Titanate Oxide, $\text{Ba}_{1-x}\text{Sr}_x\text{TiO}_3$ (BSTO), ferroelectric antennas achieve their tuning by the variation of the material properties, opposite to the microstrip antennas which achieves tuning via variations in the antenna physical structure.

The most popular ferroelectric for room temperature operation is BSTO where varying x can vary the maximum of the dielectric constant from 20°K to 395°K. Ferroelectric materials should exhibit low loss tangent over the range of operating dc bias voltages, insensitivity of dielectric properties to changes in environmental conditions and maximum reproducibility of the dielectric properties with respect to the applied DC voltage. Material characteristics showing large tunability property associated with high dielectric constant are shown below.

The capabilities of dual band multi-functional antennas have triggered intense research on microstrip antennas printed on high dielectric substrates with multi-frequency and multi-functional operations. Microstrip antennas on high permittivity substrates suffer from narrow bandwidth and poor efficiency that is due to the energy loss associated with the excitation of surface modes [10]. Passive designs that could solve this problem are generally classified into multi-resonator antennas, such as multi-layer patch antennas [11, 12]. The stacking of antenna elements could provide a solution to enhance the gain, bandwidth and introduce dual

band performance. The optimization of multi-layer antennas requires simultaneous variation of the dielectric constant, thickness of air gap, and thickness of substrate layer. No publications have been made on single layer BSTO slot or folded-slot antenna structures.

2.4.1 BSTO Publications

In [10] the behavior of a single layer BSTO antenna structure (Figure 2.11) was experimentally tested. A microstrip patch of size 4.6 cm length and 3.35 cm width was printed on a BSTO substrate of thickness 2.35 mm for operation at 0.85 GHz. The dielectric constant of the substrate before biasing was 28. When the antenna gain was measured with respect to a standard-gain log-periodic dipole a negative gain was observed as shown in Figure 2.12. Such gain value implied that the power radiated was smaller than the input power, making such antenna rather inefficient.

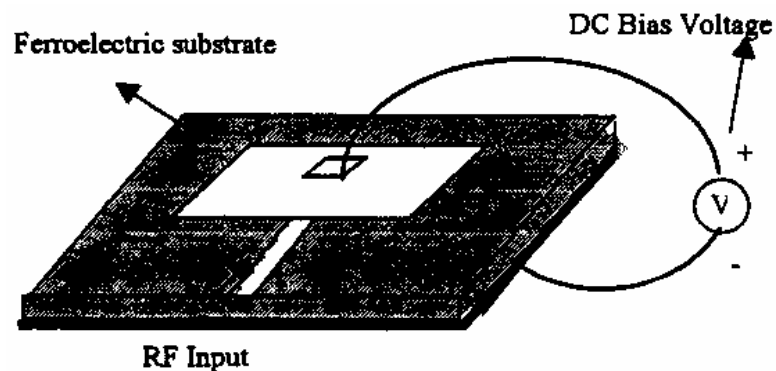


Figure 2.11. Schematic diagram of a single layer tunable BSTO ferroelectric antenna. (Taken from [10]).

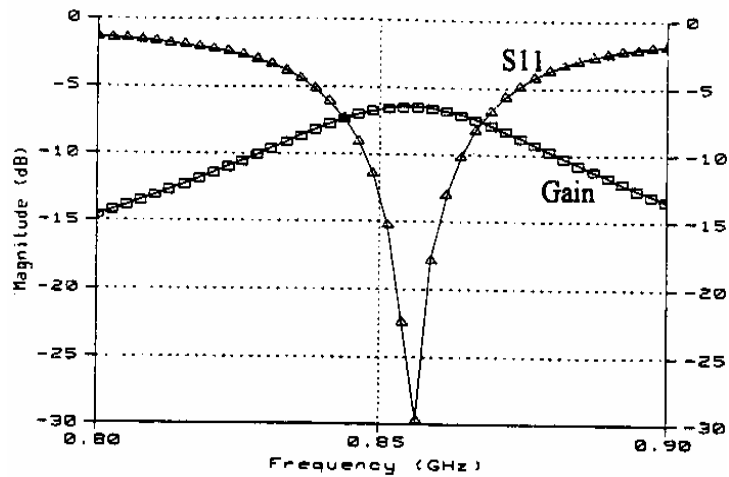
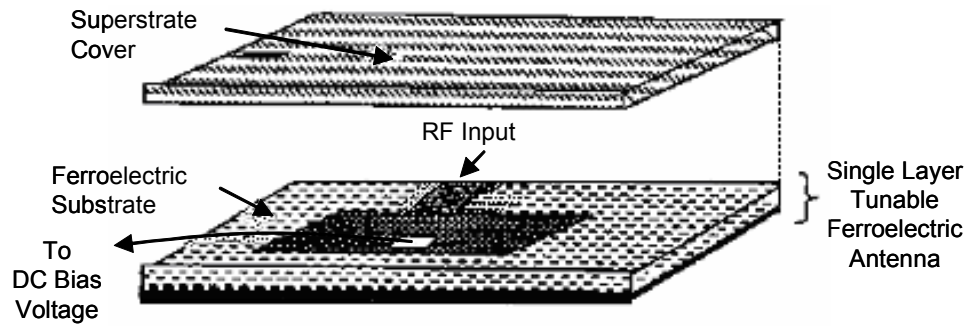
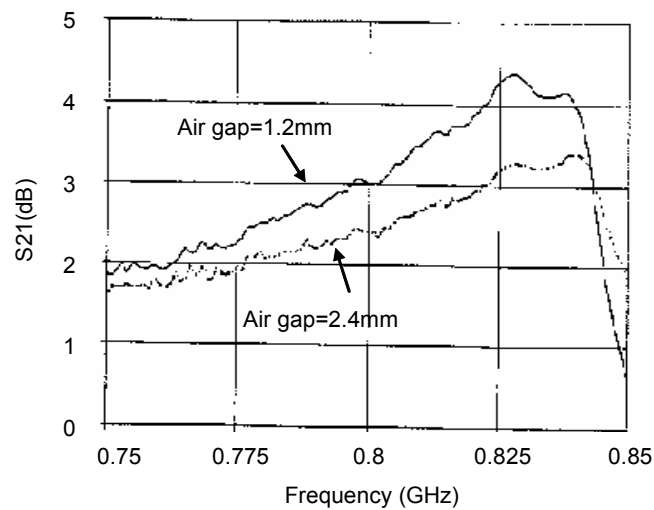


Figure 2.12. Measured unbiased reflection loss and gain performance. (Taken from [10]).

In view of the problem of an inefficient tunable ferroelectric antenna, a multi-layer structure was fabricated in [11]. In this structure an air gap separated the previous ferroelectric antenna from a superstrate cover ($h = 1.6$ mm and $\epsilon_r = 120$). Here the superstrate layer served as a protective shield and enhanced the gain of the otherwise low gain single layer structure. The air gap spacing allowed biasing connection to be set up on top of the bottom tunable layer. The structure and measured gain performance at different air gaps are presented below. Note that varying the air gap thickness optimized the structure gain. These results clearly illustrated a gain improvement of at least 5 dBi compared to the single layered structure.



(a)



(b)

Figure 2.13. Ferroelectric antenna with superstrate cover. (a) Schematic diagram. (b) Measured unbiased gain performance. (Taken from [11]).

In [11] an improved design of gain enhancement is presented, where a conductive layer was deposited on top of the superstrate cover as shown in Figure 2.14. This new structure consisted of a feeder resonator at the bottom and a parasitic radiator at the top. The parasitic radiator was etched on the superstrate cover and electromagnetically coupled to the feeder resonator. A gain improvement was observed when compared to that of the original single layer antenna. In this case, an improvement of at least 6 dBi was achieved.

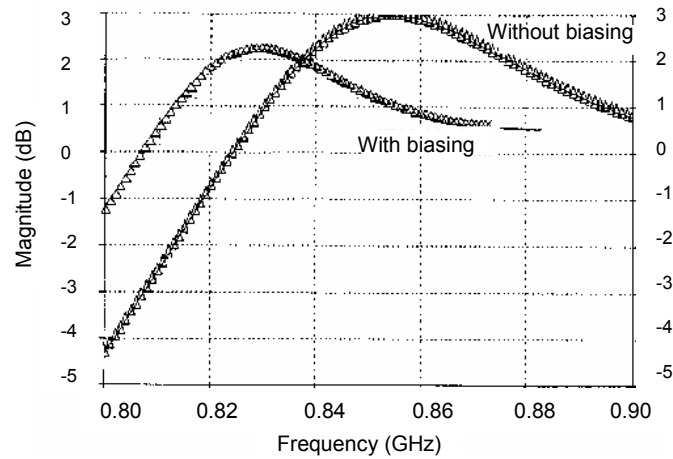
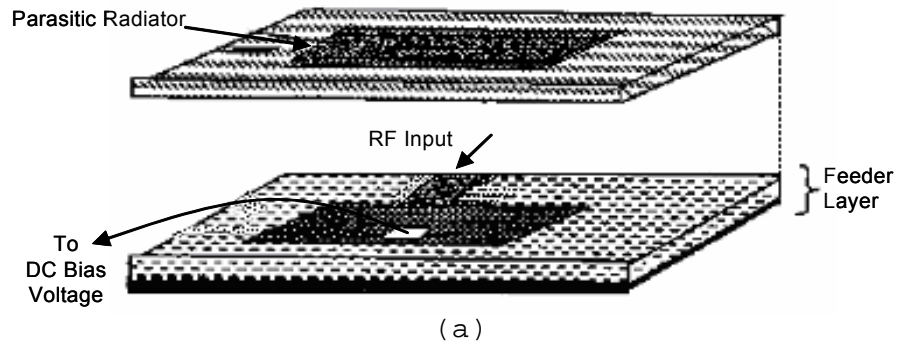


Figure 2.14. Multilayered antenna with parasitic radiator. (a) Schematic diagram. (b) Measured tunable gain performance. (Taken from [12]).

In all the previous structures air gap spacing was present, resulting less attractive for a space constrained environment. A solution was proposed in [12] by stacking the ferroelectric layer and its biasing circuitry directly on top of a conventional microstrip antenna, eliminating the air gap spacing. The feeder-radiator in this case excited electromagnetic energy for the director element and served as the ground plane for the ferroelectric substrate layer.

From Figure 2.15, the bottom patch (feeder element) designed for resonance at $f_r = 2.45$ GHz was printed on a substrate with dielectric constant (ϵ_r) of around 3. A ferroelectric material ($\epsilon_r = 79.8$) with a patch ($f_r = 3$ GHz) printed on its upper surface was placed directly on top of the feeder patch. The entire antenna structure was made tunable by applying a DC biasing voltage across the top ferroelectric substrate. As demonstrated in Figure 2.16 a gain improvement of at least 7 dBi was achieved when compared to that of the original single layer antenna.

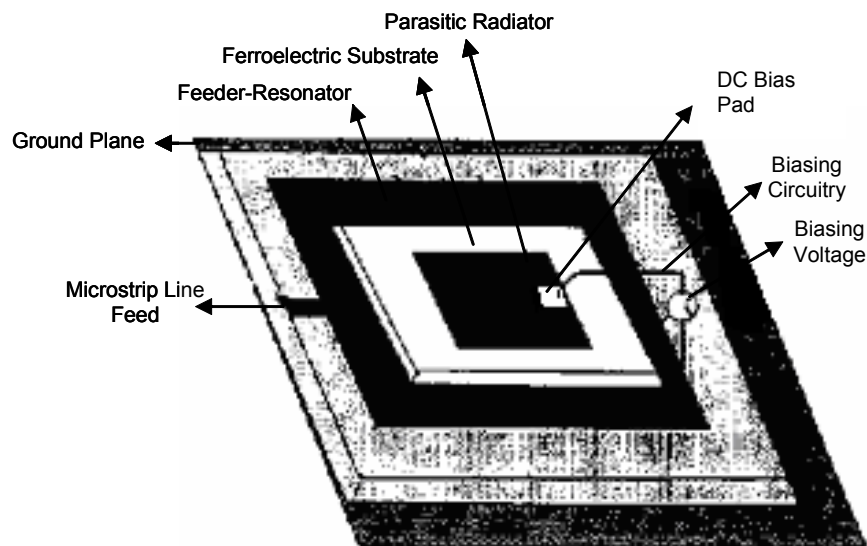


Figure 2.15. Schematic diagram of a multilayered direct stacking dual band antenna. (Taken from [12]).

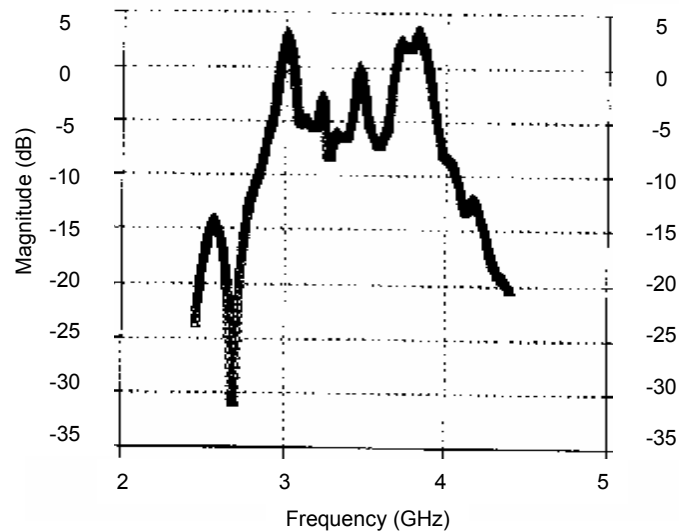


Figure 2.16. Measured unbiased gain performance. (Taken from [12]).

2.5 Simulation Software

The majority of computer aided design software for microwave planar circuits is based on models of circuit elements that are valid for a limited range of dielectric constant. Therefore designing miniaturized circuits on high dielectric constant substrates requires a full wave analysis approach. The Finite Difference Time Domain (FDTD) technique analyzes different types of planar antennas on dielectric substrates with different thickness.

A pulse excites the planar antennas. The FDTD space steps (Δx , Δy and Δz), are chosen to allow integral numbers of unit cells to fit exactly all the dimensions of the circuit. These space steps can not exceed their space limit of $2(\Delta x) > \Delta y$ and Δz , also, $\Delta < \lambda/10$. The stability of the method is assured by the Courant stability criterion. Perfect matched layer (PML) absorbing boundary conditions are implemented on all sides of the computational space to

absorb the incident wave and eliminate reflections into the computational space. After the excitation is launched, the fields are computed at successive time steps until the entire field intensities in the domain decayed to a negligible steady-state value. FDTD has been applied in the analysis of a circularly polarized slot [3] and CPW-fed folded slot on thin substrates [5] for active arrays and for circuits on high dielectric constant substrates [13].

The FDTD design specifications were not presented in [3] and [13]. In [5] a Gaussian derivative pulse ($E_x(t)$) with unit amplitude excited the CPW line. The FDTD space steps were $\Delta x = 0.3$ mm $\Delta y = 0.5$ mm and $\Delta z = 0.271$ mm and the time step used was 4 ps. The antenna structure dimensions and impedance response have been previously described. Figure 2.17 shows the computation domain used in the FDTD simulation of the CPW-fed folded-slot antenna and excited pulse.

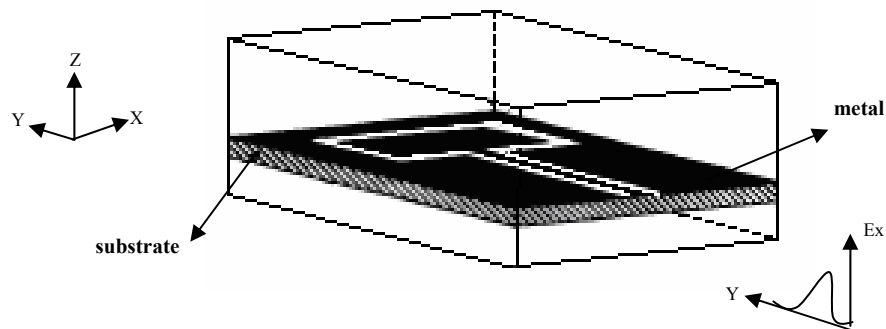


Figure 2.17. Computational domain of CPW-fed FSA. (Taken from [5]).

2.6 Chapter Conclusions

This chapter presents a literature review of the most commonly used antenna structures and ferroelectric materials at microwave frequencies. The results of previous investigative works were introduced, as well as the antenna and ferroelectric characteristics and simulation software. In the next chapter, the materials and methodology used to accomplish this thesis research will be described. The proposed antenna structures, design process, simulation software and results will be presented. The development of a design of experiment to obtain a model of the antenna structure will be also included.

CHAPTER 3

Methodology

3.1 Purpose

It is of great interest to model and experimentally verify the performance of a two-layered electrically tunable coplanar waveguide transmission line fed folded slot antenna (CPW-fed FSA) with double resonance at Ka-band. The structures schematic and its design parameters are shown in Figure 3.1 and 3.2. A thin film ferroelectric material layer is deposited on top of the substrate layer and on top of such ferroelectric layer is the ground plane, where the FSA is fed by CPW transmission lines.

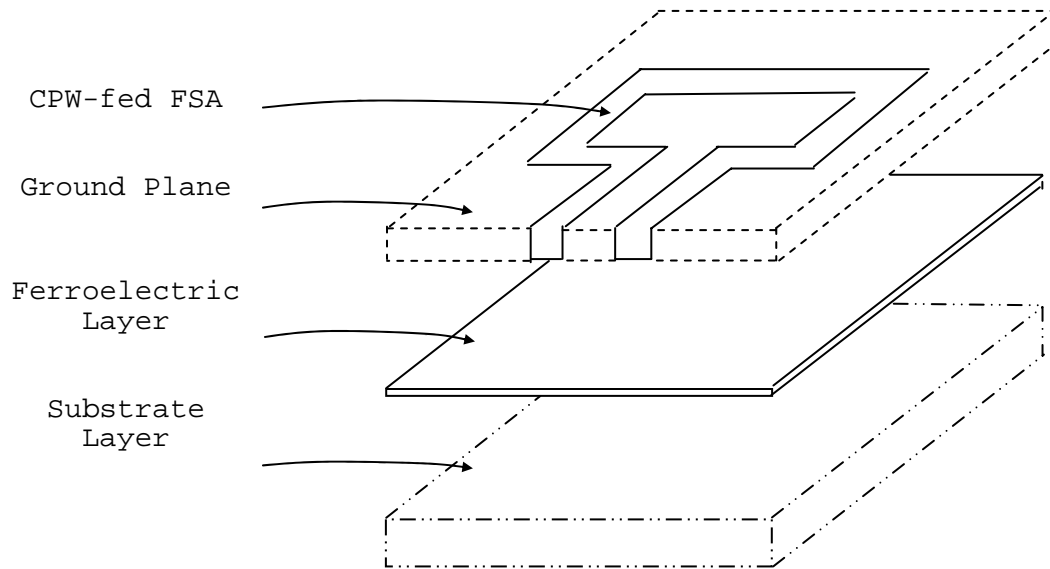


Figure 3.1. CPW-fed FSA schematic.

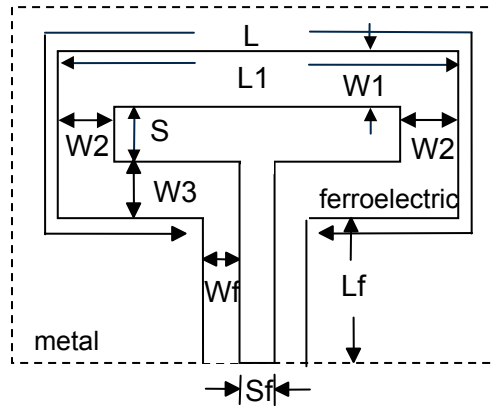


Figure 3.2. CPW-fed FSA design parameters.

The dimensions under consideration were the FSA top slot length (L_1) and the top, side and bottom slot widths (W_1 , W_2 , and W_3), the separation between the top and bottom slots (S) and the length (L_f), width (W_f) and separation (S_f) of the CPW feed. These are shown in Figure 3.2.

The materials used in the antenna configuration were: Barium Strontium Titanate Oxide, $Ba_xSr_{1-x}TiO_3$ (BSTO), a thin film ferroelectric material with a thickness of $0.4 \mu\text{m}$ and relative permittivity of 800 varied by DC biasing voltage. This material was deposited on a Magnesium Oxide (MgO) substrate with a thickness of 0.305 mm and with a relative permittivity of 9.8. The FSA metallization consisted of gold (Au) with a thickness of 2 microns.

3.2 Procedure

First, the preliminary dimensions for the antenna components were obtained and the structures were simulated with and without the ferroelectric material in order to study the effect of this film on the structure. Second, the antenna with the applied ferroelectric material was matched to 50 ohms and its optimum dimensions were obtained through

a design of experiment. Also, the film relative permittivity was changed and its effect on the output responses studied. Goal-models were generated for the desired structure output responses. And finally, a prototype was fabricated for validation purposes.

3.3 Simulation Software

The use of simulation software was essential in order to achieve our goals. Software, such as LineCalc by Advanced Design System was used to obtain preliminary design dimensions; the Finite Difference Time Domain (XFDTD) software by Remcom, Inc. was used to simulate all the antenna structures in order to obtain the output responses. The Design Expert software by Stat-Ease was used to obtain a goal-model of the optimum dimensions and output responses for the desired structure.

3.3.1 LineCalc Software

The preliminary antenna dimensions were calculated through LineCalc. This software required as input, the substrate relative permittivity (9.8) and thickness (0.305 mm) and the matching resonant frequency (30 GHz). Our desired preliminary dimensions were obtained from CPW transmission lines. In order to calculate these dimensions, the software allows you to either fix the separation between the transmission lines (G) or its width (W) to a desired dimension. It was decided to fix G at 0.249 mm. The line characteristic impedance ($Z_0 = 50$ ohms) and electric length ($\phi = 180^\circ$) of the CPW transmission lines were synthesized in order to obtain its width (W) and length (L). An electric

length of 180° was used because the antenna length, L , is approximately $\lambda/2$.

3.3.2 XFDTD Software

The antenna structures were simulated in XFDTD. Among many numerical techniques for electromagnetic problems, the FDTD method was selected for this work because it can handle a variety of circuit configurations with a minimal amount of programming effort. Also, it analyzes different types of planar antennas on dielectric substrates with different thickness.

3.3.2.1 FDTD Method

A Gaussian derivative pulse with unit amplitude given by,

$$Ex(t) = e^{2((t-t_0)^2/T^2)^2} \quad (3.1)$$

was excited in the CPW line, where T was the pulse half width in the time domain and $t_0=4T$. The maximum frequency from the Gaussian spectrum that can be relied on is $f_{max}=1/2T$. The FDTD space steps, Δx (0.083 mm), Δy (0.0625 mm), Δz (0.0762 mm), were chosen to allow integral numbers of unit cells to fit exactly all the dimensions of the circuit. These space steps were obtained from the smallest slot width and the total material thickness, given by,

$$\Delta x, \Delta y = \frac{\text{slot_width}}{\text{unit_cells}} \quad \Delta z = \frac{h_f + h_s}{\text{unit_cells}} \quad (3.2)$$

where h_f and h_s were the ferroelectric and substrate material thickness. These space steps can not exceed their space limit which was $2(\Delta x) > \Delta y$ and Δz , also, $\Delta < \lambda/10$. The stability of the method was assured by the Courant stability criterion,

$$\Delta t = \frac{kc}{\sqrt{\left(\frac{1}{\Delta x}\right)^2 + \left(\frac{1}{\Delta y}\right)^2 + \left(\frac{1}{\Delta z}\right)^2}} \quad (3.3)$$

where k is the Courant factor and c is the speed of light.

Another aspect required for accuracy in the results is the refinement of the mesh. Although this method uses minimal amount of programming effort, the calculation of the mesh at each layer may required more run time due to the small thickness of the BSTO material. To minimize the run time, an average of the relative permittivities at each interface was calculated. Since the selected space step Δz was much larger than the thickness of the BSTO layer, the unit cells at the top of the ferroelectric-substrate interface were given an effective relative permittivity. This permittivity was calculated using a weighted average of the MgO and BSTO relative permittivities used in [13], given by,

$$\varepsilon_{avg_{fs}} = \varepsilon_{rf} \left(\frac{h_f}{\Delta z} \right) + \varepsilon_{rs} \left(1 - \frac{h_f}{\Delta z} \right) \quad (3.4)$$

where ε_{rf} and h_f were the ferroelectric relative permittivity and thickness, ε_{rs} was the substrate relative permittivity and Δz was the space step in the z-direction. An average of the permittivity at the bottom air-substrate interface, $(\varepsilon_{rs}+1)/2$, was used as explained in [14].

Perfect matching layer (PML) absorbing boundary conditions were implemented on all sides of the antenna structure to absorb the incident wave and eliminate reflections. After the excitation was launched, the fields were computed at successive time steps until the entire field intensities in the domain decayed to a negligible steady-state value.

3.3.3 Design Expert Software

The Design Expert software was used to obtain a goal-model of the output responses for the desired structure. A geometrical design with k input factors was used for the goal-model design process. The geometrical design allows input factors to have different number of levels represented by coefficients. The representation of each level facilitates the adjustment of a regression model that relates the output response with the input factor levels. It will create an experiment that includes all possible combinations of the input factor levels. These designs have a simplified analysis, and they also are the basis of many other useful designs.

3.3.3.1 Geometrical Design

The geometrical design used consisted of a combination of two and three level factorial designs. The two-level factorial design had k input factors at low and high levels, represented by -1 and 1. Because each complete replicate of the design has 2^k runs, the arrangement is called a 2^k factorial design. The input factors considered in this factorial design were the widths of the FSA and the separation between the top and bottom slots. The 3^k factorial design is a factorial arrangement of k input

factors that each have three levels. These input factor levels are low, center and high, represented by -1, 0 and 1. The input factor considered in this factorial design was the thin film relative permittivity.

With these 5 input factors a geometrical design of $2^4 3^1$ combinations were obtained for a total of 48 design combinations. This design allows five main effects to be estimated (S , ϵ_{rf} , $W1$, $W2$ and $W3$) along with ten two-factor interactions ($S\epsilon_{rf}$, $SW1$, $SW2$, $SW3$, $\epsilon_{rf}W1$, $\epsilon_{rf}W2$, $\epsilon_{rf}W3$, $W1W2$, $W1W3$ and $W2W3$), six three-factor interactions ($S\epsilon_{rf}W1$, $S\epsilon_{rf}W2$, $S\epsilon_{rf}W3$, $\epsilon_{rf}W1W2$, $\epsilon_{rf}W1W3$ and $W1W2W3$), two four-factor interactions ($S\epsilon_{rf}W1W2$, $S\epsilon_{rf}W1W3$) and a five-factor interaction ($S\epsilon_{rf}W1W2W3$). When all the input factors of an experiment are fixed, it is easy to formulate and prove hypothesis about the principal effects and interactions.

3.3.3.2 Goal-model Design Process

The output responses were analyzed through an input factor effects list. This list presented the input factors effects and contribution percentage for each output response. The prediction equation generated through ANOVA was used as the goal-model. The simplified model yielded an equation in terms of the input factors and for each output response. Each equation that was generated consisted of the effect that those factors had on the output responses. With such equations each output response can be estimated without the need of an electromagnetic simulator. They also may be the basis for analyzing preliminary design dimensions for a CPW-fed FSA before simulation.

3.4 Design Dimensions

A model of a CPW-fed FSA without the thin ferroelectric material was used to obtain preliminary dimensions for the antenna structure through LineCalc. The preliminary dimensions for a FSA were obtained from coplanar waveguide transmission lines and applied to the CPW-fed FSA structure. The CPW length obtained was applied as the structures overall length. This Symmetric Folded Slot Antenna (SFSA) structure was simulated in XFDTD, serving as base for comparison between the structures with and without the ferroelectric material.

A matching at 50 ohms with a frequency of 30 GHz was intended for this CPW-fed FSA. Towards this end, the top slot width of the SFSA with the applied ferroelectric material was varied in order to match the antenna. Through the impedance matching technique (IMT) presented in [1], this width can be increased to reduce the input impedance of the antenna to 50 ohms. An increase in this width causes a shift in the resonant frequency and therefore, in the output responses. Such changes in dimension yields an Asymmetric Folded Slot Antenna (AFSA). The pertinent antenna dimensions need to be found for this AFSA to comply with the desired design specifications. All proceeding simulations were completed for this AFSA and will be referred as the FSA.

3.5 Design of Experiment

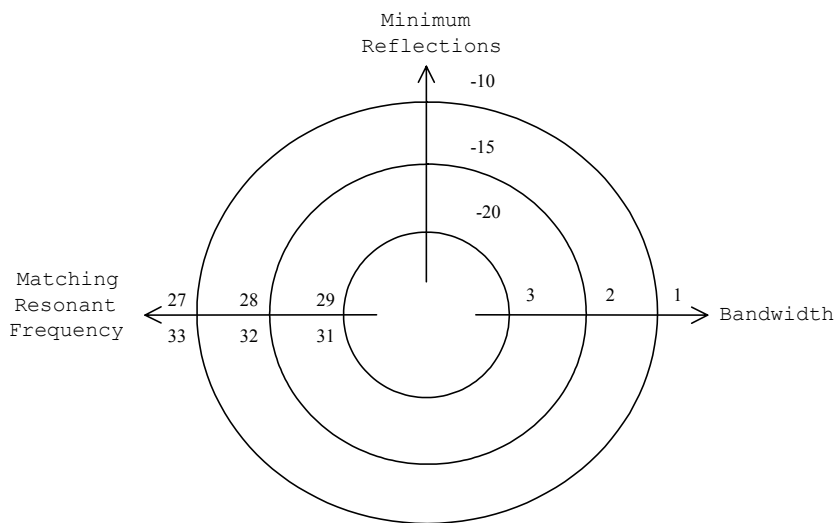
The primary goal in scientific research is usually to show the statistical significance of the effect that a particular factor has on the desired dependent variable. The traditional approach of collecting data by holding each factor constant until all possibilities have been tested becomes impossible as the number of factors increases. It is of great interest to maximize the information that can be extracted from our FSA with the least amount of runs. The process of obtaining the desired output responses may be quite time consuming if it is not done in an organized manner. Therefore, for this purpose the simulation runs were chosen from the statistic technique, Design of Experiments (DoE).

In this type of antenna structure, the input factors are usually physical dimensions and the output factors such as the reflections, bandwidth, input impedance and gain are dependent of frequency. The five input factors that were considered in this DoE were the widths of the FSA, the separation between the top and bottom slots and the relative permittivity of the BSTO film. The first input factors were varied at a low and high level, represented with a -1 and +1. The last input factor was varied at low, center and high levels, represented by -1, 0 and +1. Geometrically, the design is a square as can be seen below.

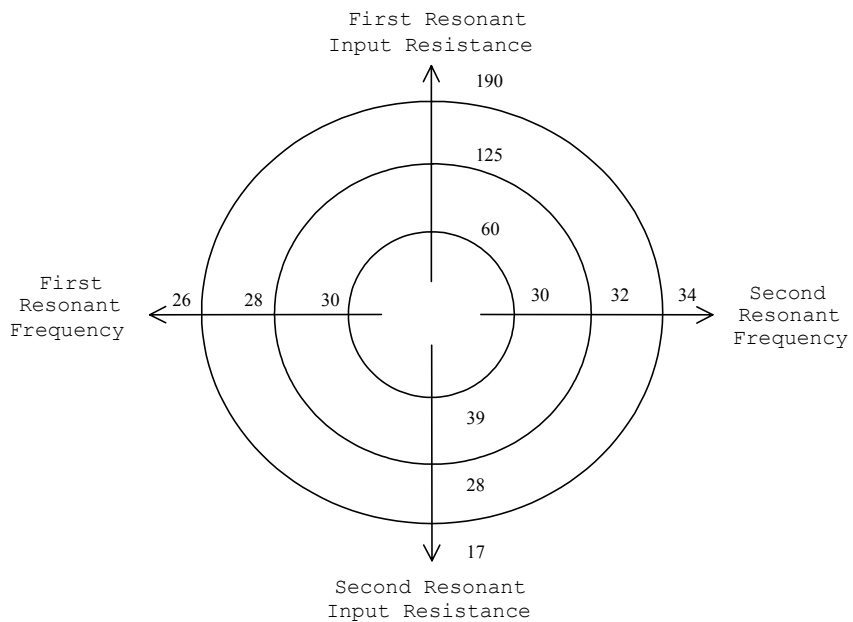
From this figure we can appreciate that the factors that laid on the X and Y axis of the big cube were the separation between the top and the bottom slots and the top slot width. The factors that laid on the X and Y axis of the small squares were the widths of the FSA bottom and side slots. These squares were repeated at the thin film relative permittivity levels. Each corner of the small squares represented a design or simulation run. A total of forty-eight simulation runs were performed in XFDTD.

The data collected from these designs was used to develop a goal-model through the Design Expert program. The simplified model yields an equation in terms of the input factors and for each output response. Each equation that was generated consisted of the contribution that these input factors had on the output responses. The data can be tabulated or graphically represented for easy interpretation of the output responses.

The graphical visualization results difficult when more than one output response and many input factors are under consideration. Therefore the Bull's Eye graphical representation [15] of the results was used. The advantage of this type of graph is easy interpretation of the results when more than two output responses are analyzed. In the case of the performed simulations, this type of graph was useful in analyzing seven output responses at three thin film relative permittivities. Figure 3.4 shows the Bull's Eye representation of the output responses.



(a)



(b)

Figure 3.4. Bull's Eye graphical representation of the output responses (a) Goal response representation. (b) Dual resonance behavior.

These Bull's Eye plots represented the goal responses and dual resonance behavior. Each axis represented an output response. In the goal response graph, the vertical axis represented the minimum reflections in dB, the left of the horizontal axis represented the matching resonant frequency in GHz and the right represented the bandwidth in GHz. The results of the corresponding output responses were represented with a point on the graph. Any point in or close to the center of the graph indicates that the goal is achieved. Therefore, the antenna performance improves as the results tend to the center of the graph.

In the dual resonance behavior graph, the top and bottom of the vertical axis represented the first and second resonant input resistance in ohms. The left and right of the horizontal axis represented the first and second resonant frequency in GHz. These results were also represented with a point on the graph. Any point in or close to the center of the graph does not indicate an improvement in the antenna performance. In this graph no goal is set; its purpose is to study the dual resonance behavior.

It was demonstrated through simulations that the resonant frequencies and input resistances of the DoE designs varied for each thin film relative permittivity. An increase in the relative permittivity of the thin film caused the resonant frequencies to decrease by 1 GHz and the first and second resonant input resistances to increase by 20 ohms and decrease by 3 ohms respectively. This behavior was observed because the fields tend to concentrate more in the substrate.

3.6 Prototype Fabrication

The prototype films were deposited by Pulsed Laser Deposition (PLD) and their lattice parameters were measured at the UPRM Department of Physics. It was intended to fabricate the CPW-fed FSA at the UPR Department of Physics by depositing a thin Au layer with an electron-beam evaporator through a lift-off mask, but due to problems with the equipment the antenna fabrication was not feasible. The prototype measurements were meant to be taken at the UPRM ECE Radiation Laboratory in order to validate the simulations.

3.6.1 PLD Technique

Today there exist several methods for preparing thin films, both physical and chemical. The physical methods can be divided into thermal evaporation and sputtering and the chemical into vapor phase and liquid phase [16]. In this work BSTO thin films were grown by PLD a physical method by thermal evaporation. PLD provides unique advantages for multicomponent oxide films because it easily reproduces the stoichiometry of the target in the deposited film.

The PLD technique uses the laser pulse to highly energize the target material, causing its surface to explode. This explosion throws out the evaporated material, which is called the plume. The reach and shape of the plume can be controlled by changing either the laser fluence or deposition pressure. The laser fluence is the energy per area (J/cm^2) of the laser spot hitting the target. It can be varied by either changing the laser pulse energy or by adjusting the laser spot size. An increase in the laser deposition pressure affects the plume by causing it to have more gas molecules to collide with and thereby not allowing

it to reach as far. The deposition pressure and atmosphere varies with the type of film being deposited. The substrate temperature is a key parameter, especially when it comes to making high quality films. Figure 3.5 shows the inside of the deposition chamber as the laser pulse hits the target.

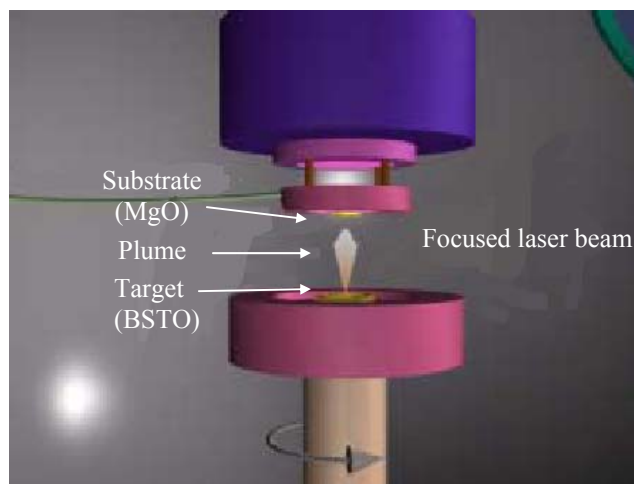


Figure 3.5. PLD process. Inside of the deposition chamber.
(Taken from [16])

The main PLD parameters are substrate temperature, laser fluence, target-substrate distance, type of gas atmosphere and deposition pressure. Since the parameters are very few, it makes the PLD technique a very attractive research tool.

$(\text{Ba}_{0.60}\text{Sr}_{0.40})\text{TiO}_3$ targets ($h_f = 0.4 \mu\text{m}$) with density of 4.9 g/cc from Praxair Surface Technologies were deposited onto (100) MgO single crystals substrates from Minicrystals. A Ba:Sr ratio of 60:40 was used because samples with higher Ba content have higher Curie temperature usually leading to higher tuning at room temperature. Prior to PLD the substrates underwent a cleaning cycle, which included an

ultrasonic cycle of trichloroethylene followed by acetone and methanol for 10 minutes each. The samples were then rinsed with methanol and nitrogen dried.

A krypton-fluoride excimer laser (248 nm, 30 ns, 30 kV) was focused on the target with laser pulse fluence of 2.3 J/cm^2 in flowing O_2 at a partial pressure of 30 mTorr and flux of 5 sccm. The deposition substrate temperature was calculated by Equation 3.5 in order to obtain the maximum substrate temperature possible with the available heater.

$$T_{\text{subs}} = (T_{\text{heater}} * 0.77) - 21.4 \quad (3.5)$$

An on-axis deposition with rotating film technique was used and lasted 30 minutes. The target was rotated to make use of as much as possible of the target area since the laser spot usually has the dimensions of a couple of millimeters. The distance between the lens and the port is 6.35 cm. The substrate was parallel to target and their separation distance was maintained at 4 cm.

3.7 Film Characterization

The lattice parameters of BSTO/MgO films were measured using a Bruker D8 Discover X-ray diffractometer using $\text{Cu K}\alpha$ radiation ($\lambda=1.5415 \text{ \AA}$). The sample interval was 0.01° and the scan beam was 0.3 seconds per step. A θ - 2θ scan of the sample was performed to observe the X-ray diffraction (XRD) peaks of intensity regarding the crystals structure. This scan provides structural information related to the lattice parameter along the film surface normal direction.

In order for the X-ray diffraction (XRD) peaks to be observed the condition for maximum intensity contained in

Bragg's Law has to be fulfilled. This allows us to calculate details about the crystal structure. Bragg's Law can easily be derived by considering the conditions necessary to make the phases of the beams coincide when the incident angle (θ) equals the reflecting angle (θ) and the path length difference between beams equals an integer of wavelengths. Below is the visualization of Bragg's Law.

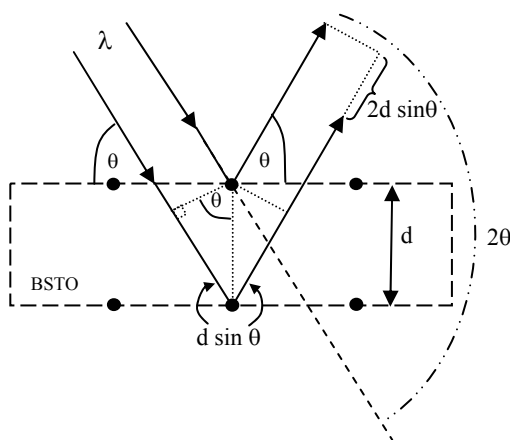


Figure 3.6. Visualization of Bragg's Law.

This figure shows two X-rays incident on two atomic layers of a crystal, separated by the distance d . The X-rays begin in phase and parallel up to the point at which the top beam strikes the top layer. When Bragg's Law is satisfied diffraction occurs. The lower beam continues to the next layer where it strikes the bottom layer. The lower beam must travel an extra distance ($2d \sin \theta$) to continue traveling parallel and adjacent to the top beam. This extra distance must be an integral (n) multiple of the wavelength (λ) for the phases of the two beams to be the same. Such conditions derive Bragg's Law given by,

$$n\lambda = 2d \sin \theta \quad (3.6)$$

It was intended to measure the structure tunability (τ) and frequency tunability factor (τ_f) determined by [17],

$$\tau = \frac{\varepsilon_{rf}(E) - \varepsilon_{rf}(0)}{\varepsilon_{rf}(E)} \quad \tau_f = \frac{f_{V_{\max}} - f_o}{f_o} \quad (3.7)$$

where $\varepsilon_{rf}(E)$ is the relative dielectric constant of the ferroelectric under an external DC field with respect to that at no field ($\varepsilon_{rf}(0)$) and f_o and $f_{V_{\max}}$ is the center frequency of the frequency agile component at no bias and at the maximum applied bias respectively. The microwave property data was intended to be collected using a HP 8510C-network analyzer with S-parameter test scanned through the frequency range of 20 to 40 GHz using a FSA fabricated from depositing a thin Au layer by electron-beam evaporation through a lift-off mask.

3.8 Chapter Conclusions

In this chapter the materials and methodology used to accomplish the research were described. The proposed antenna structures, design process, simulation software and prototype fabrication and measurements were presented. In the next chapter the results will be presented, analyzed and explained.

CHAPTER 4

Results and Discussions

4.1 Preliminary Dimensions

The preliminary dimensions for the coplanar waveguide (CPW) fed folded slot antenna (FSA) structure were obtained from the dimensions of (CPW) transmission lines. These dimensions were used to model the CPW-fed FSA structure without the thin ferroelectric material. The obtained CPW length (L) was applied as the structures overall length. The CPW transmission line length, width (W) and gap (G) dimensions obtained from LineCalc are shown in the following table.

Table 4.1
CPW Feed Dimensions

Parameters	Dimensions (mm)
L	2.61
W	1.083
G	0.249

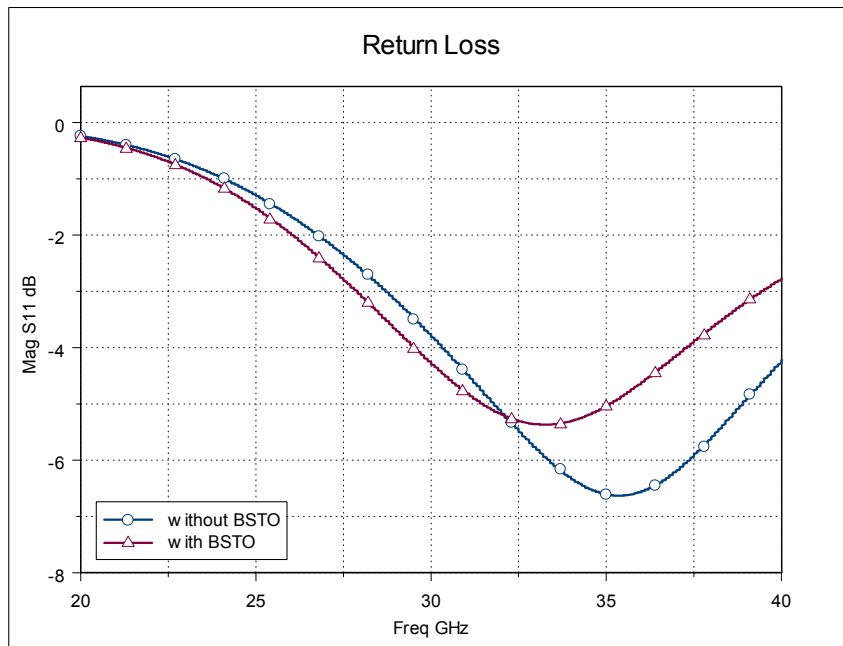
The width of the transmission line was modified in order to simulate the antenna structure. Such modification was necessary because the widths of the CPW transmission lines (2.166 mm) left little space in the x-direction for the unit cells corresponding to the FSA. After simulation it was found that the overall length was quite small for the FSA to resonate at 30 GHz and, therefore, it was modified. These parameters were given new values since it was not intended to obtain input impedance (Z_{in}) of 50 ohms by varying the dimensions of the CPW transmission line,

although the structure matching was achieved later by other means.

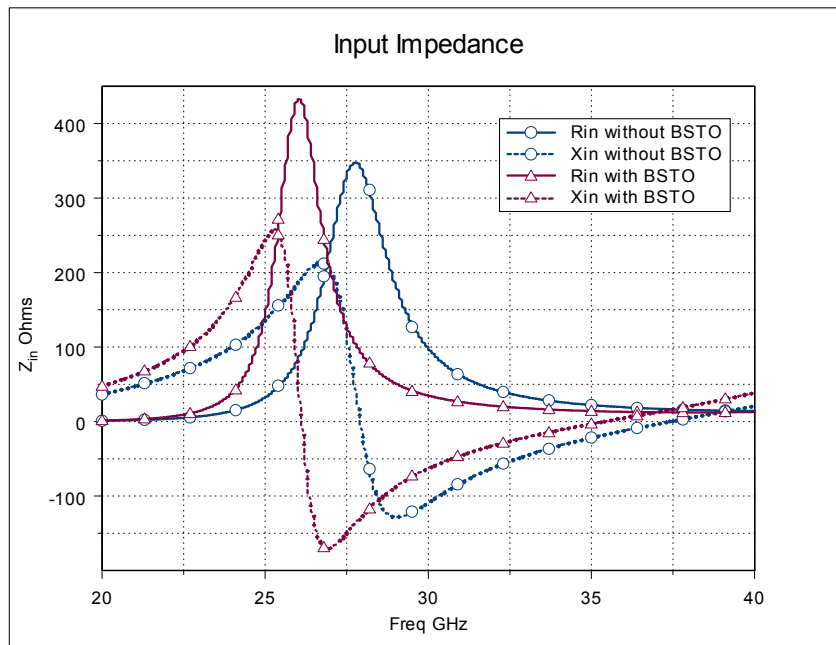
The resulting structure was a Symmetric Folded Slot Antenna (SFSA) do to the equality in its widths. The SFSA dimensions slightly differ since integral numbers of unit cells have to fit exactly all the dimensions of the structure when simulating in XFDTD. The antenna structure was simulated with and without the ferroelectric material, as presented in Figure 4.1, in order to study the effect of this film on the structure. Table 4.2 shows the preliminary dimensions used for the folded slot antenna and the new CPW transmission line dimensions.

Table 4.2
SFSA Preliminary Dimensions

Parameters	Dimensions (mm)
L	4.691
L1	1.909
W1	0.25
W2	0.249
W3	0.25
S	0.249
Lf	0.1875
Wf	0.083
Sf	0.249



(a)



(b)

Figure 4.1. SFSA simulated results with and without the applied ferroelectric material. (a) Return Loss. (b) Input Impedance. (c) Elevation pattern.

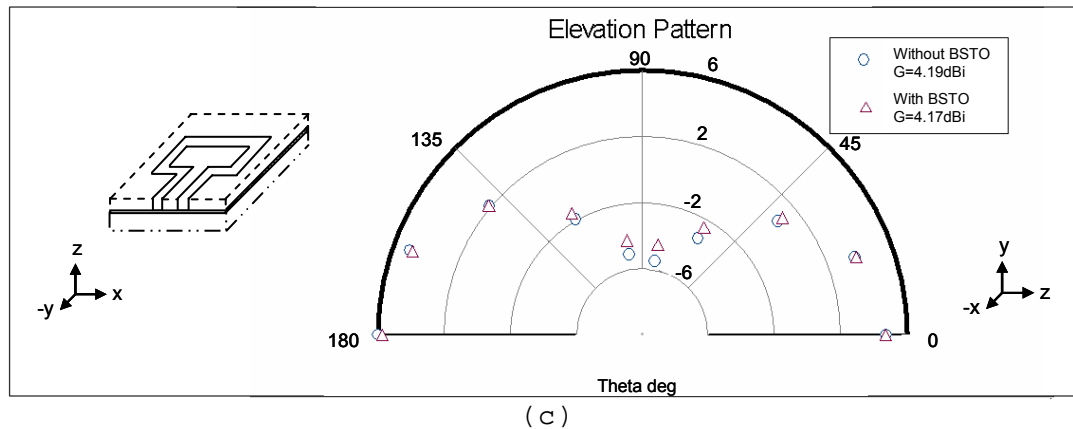


Figure 4.1. Continued

The effect of this film on the antenna structure was the reduction in the matching resonant frequency and an increase in the reflections as well as in the input impedance. At the dual resonance, which occurs at zero reactance, we note that at the first resonant frequency the input resistance increased and at the second resonant frequency it decreased. The first and second resonant frequencies had a difference of 10 GHz.

Note from Figure 4.1 c, that the antenna is located parallel to the YZ plane with the substrate layer towards the left of the graph and the metallization layer towards the right. The graph shows that the electric fields concentrate more in the substrate layer, which acts as a cavity. The remaining elevation patterns of this thesis were obtained with the same antenna location.

A 4.19 dBi gain at $\theta=0^\circ$ was observed for the structure with the BSTO film and a gain of 4.17 dBi for the structure without the BSTO film. The gain of the structure seemed almost not affected by the applied film. Generally the gain of a slot antenna is about 1.6 dBi and the SFSA is approximately 4.19 dBi.

4.2 Matching Dimensions

The structure with the applied ferroelectric material was matched by increasing its width $W1$, to reduce its input impedance to 50 ohms. An increase in $W1$ causes a shift in the output responses. Changes in the structure dimensions were made in order to compensate for the encountered shift. Such changes in dimension yields an Asymmetric Folded Slot Antenna (AFSA) and are studied in Figures 4.2 through 4.5.

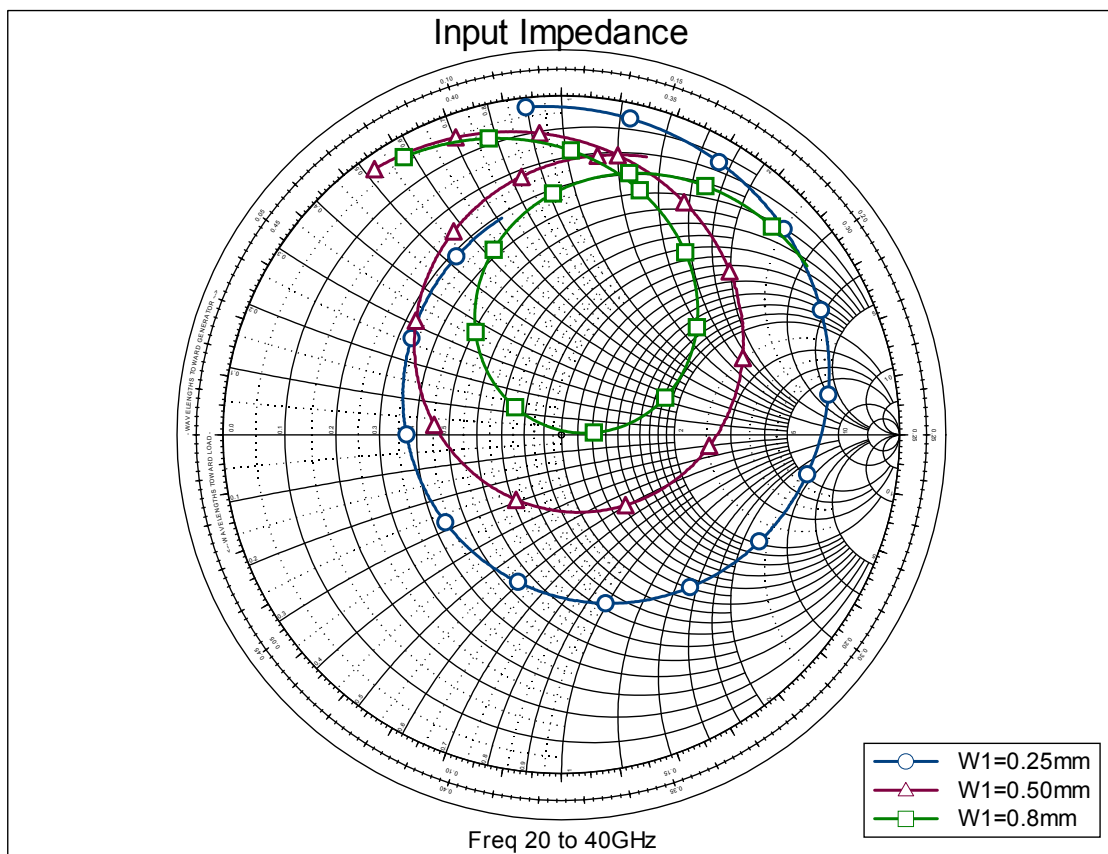


Figure 4.2. Top slot width variation.

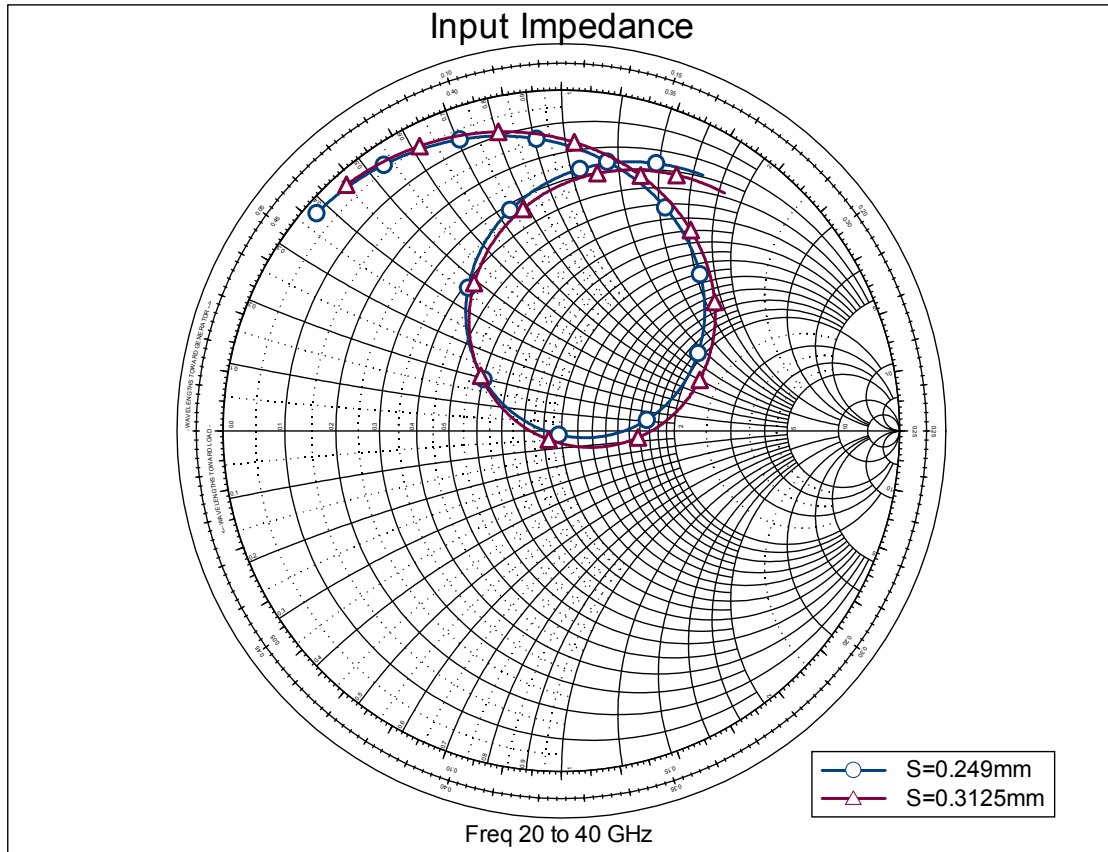


Figure 4.3. Separation between top and bottom slot width variation.

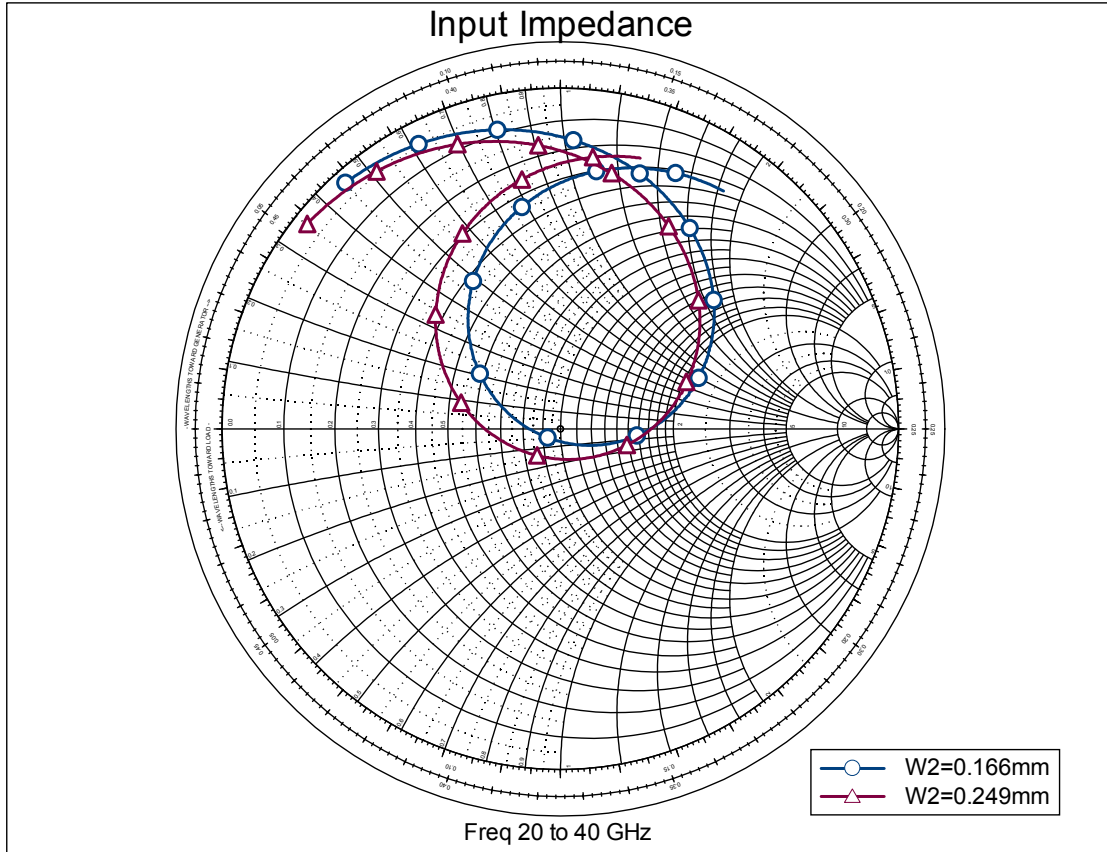


Figure 4.4. Side slot width variation.

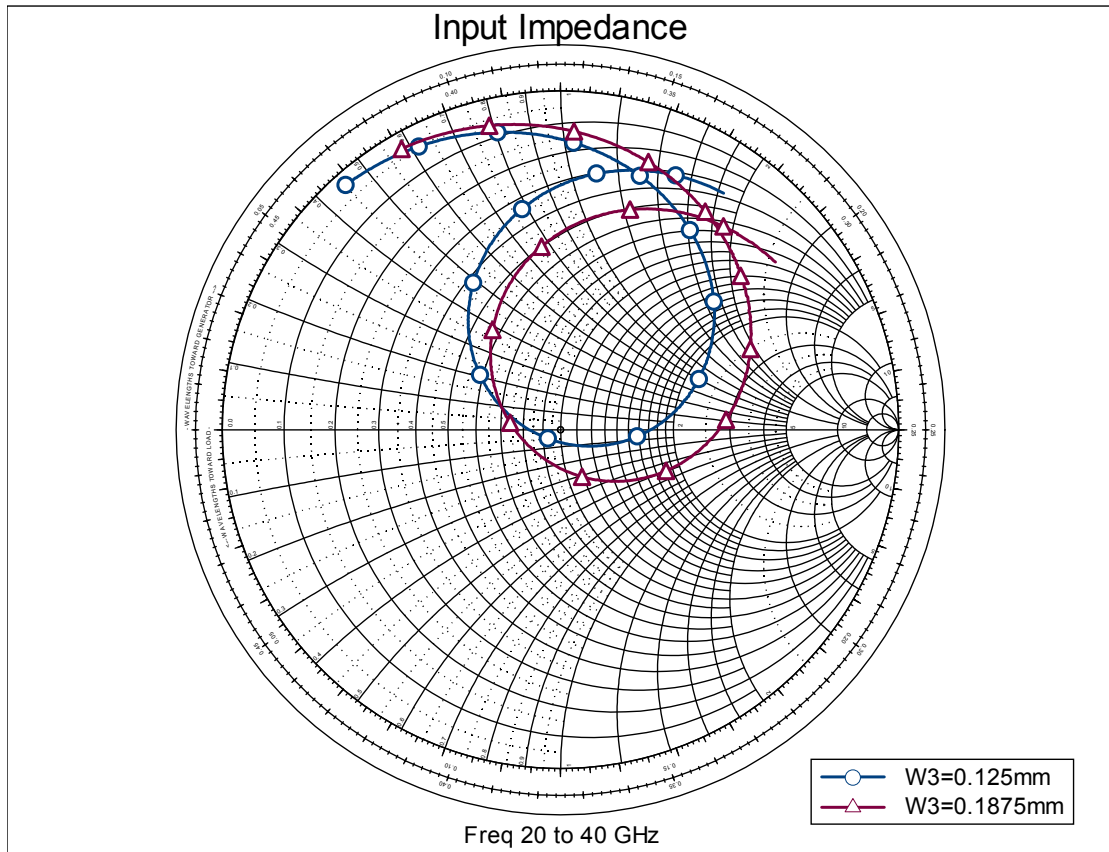


Figure 4.5. Bottom slot width variation.

Changes in the structures widths demonstrated an effect on the input impedance. An increment in the top slot width ($W1$) dimension caused the input impedance to decrease and the antenna matched to 50 ohms. Changes in the structures separation between the top and bottom widths (S) and in the side ($W2$) and bottom ($W3$) slot widths demonstrated an opposite effect on the input impedance. The input impedance loops of $W2$, $W3$ and S increased with dimension. The input impedance loop of $W2$ shifted to the second resonance region (left region on the Smith Chart) and the input impedance loop of $W3$ shifted to the first resonance region (right region on the Smith Chart), as well as well as the input impedance loop of S although slighter.

It was observed that $W2$ and $W3$ had opposite and very noticeable effects. The effect of S was more opposite to $W1$. With these observations noted it was desired to obtain an input impedance loop as thin as possible in order to obtain a wide bandwidth. The pertinent changes to the previous dimensions were considered and the matching dimensions for the AFSA are tabulated in Table 4.3. The output responses for the AFSA and the SFSA are compared in Figures 4.6 and 4.7.

Table 4.3
AFSA Matching Dimensions

Parameters	Dimensions (mm)
L	4.859
L1	2.158
W1	0.75
W2	0.166
W3	0.125
S	0.3125
Lf	0.1875
Wf	0.083
Sf	0.249

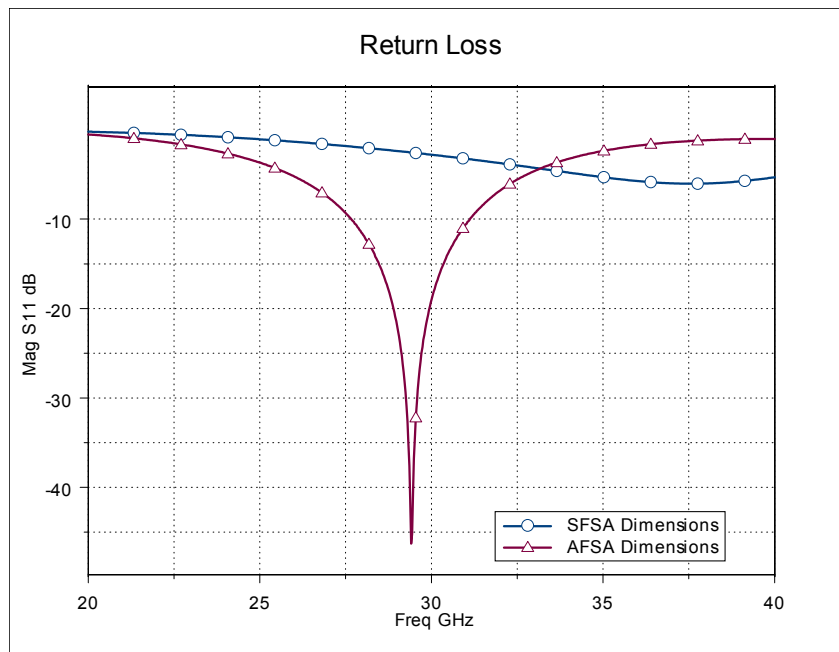
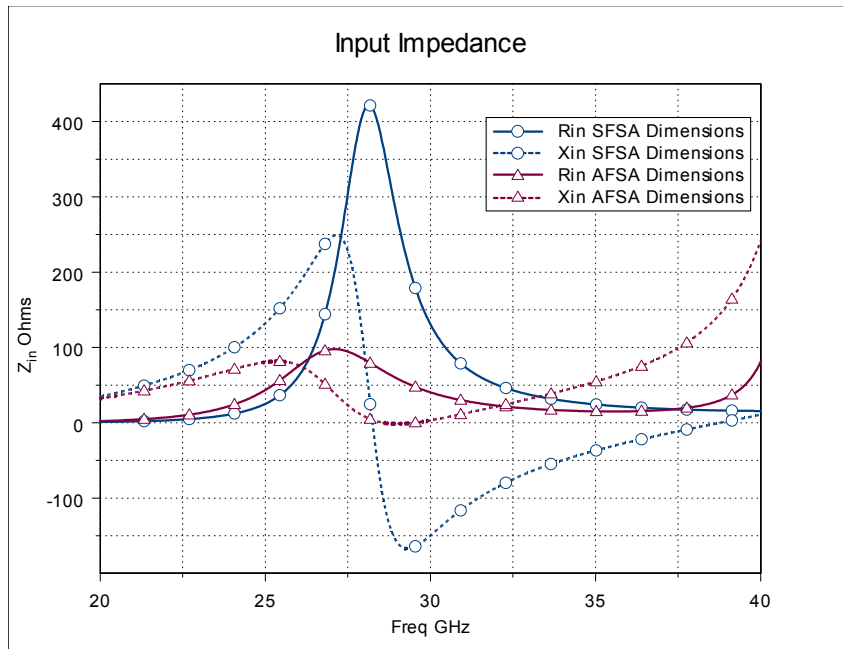
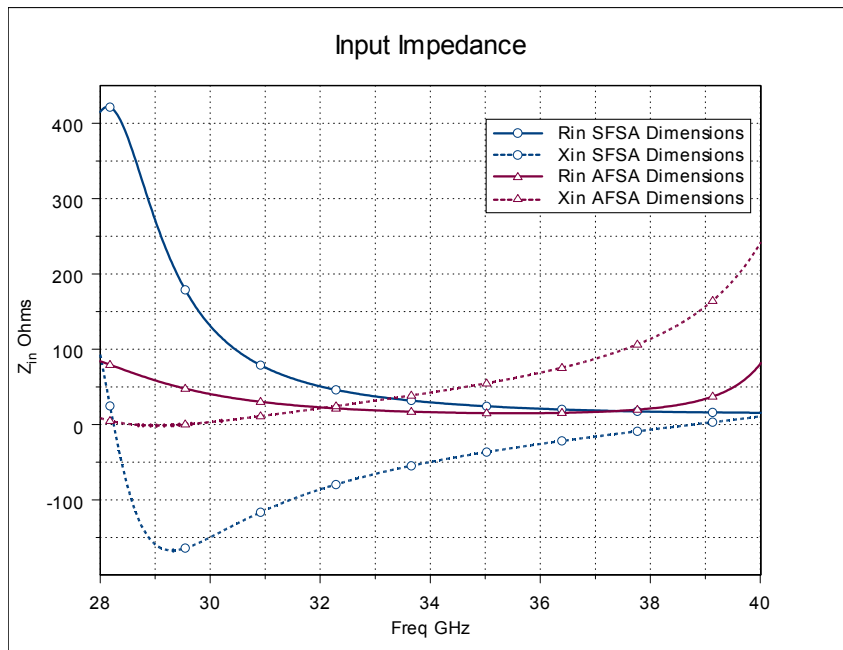


Figure 4.6. Simulated return loss of the preliminary and matching dimensions.



(a)



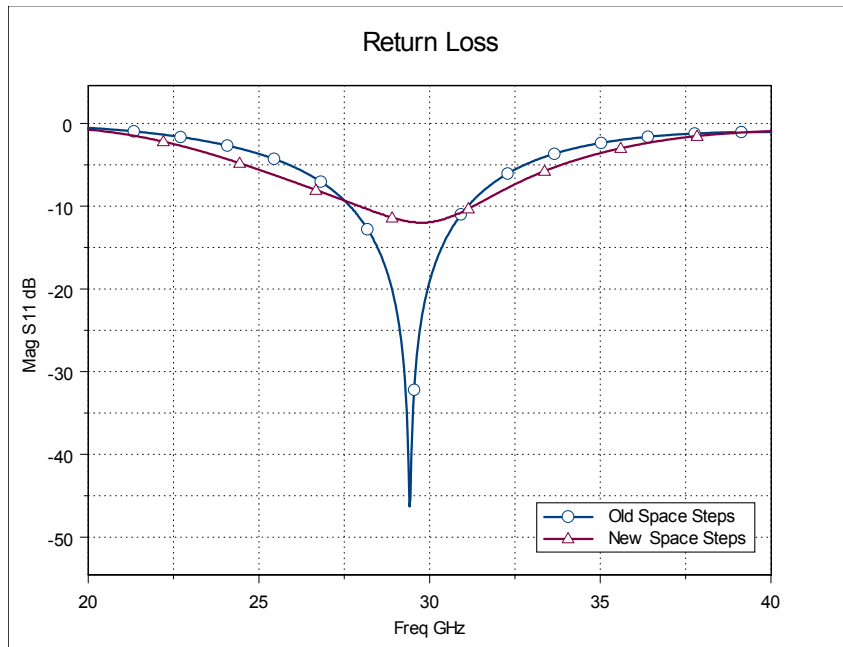
(b)

Figure 4.7. Simulated input impedance of the preliminary and matching dimensions. (a) Full frequency range. (b) Zoomed frequency range.

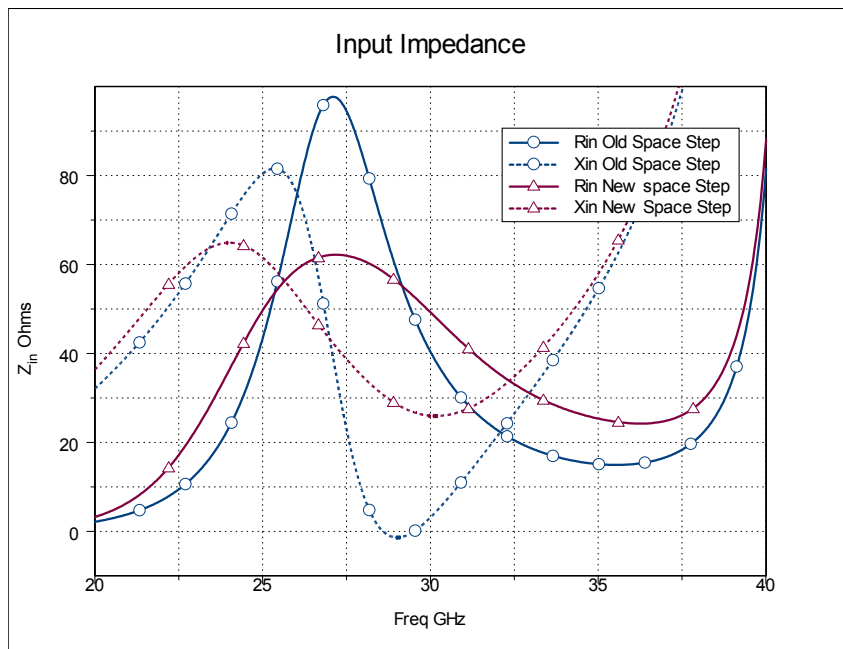
The SFSA resonated at 29.00 GHz with high reflections of -3.7 dB. Its dual resonance occurred at 26.08 and 35.35 GHz for a wide input resistance range between 13.72 and 427.67 ohms. Note that, with the use of the IMT and the variations in antenna dimensions, the produced AFSA complied with the desired objectives. The AFSA resonated at 29.38 at minimum reflections of -45 dB and bandwidth of 3.5 GHz. Its dual resonance occurred at 28.55 and 29.46 GHz for a compact input resistance range between 48.57 and 68.54 ohms.

4.3 Space Step Variation

It was decided to decrease XFDTDs space steps in order to refine the mesh at the ferroelectric-substrate interface, and therefore, validate the weighted average equation used at this interface. The X space step (Δx) was varied because the largest antenna dimension was in this direction. The Z space step (Δz) was varied because the largest unit cells were occupied in this direction. The Y space step (Δy) remained unchanged. The X and Z space steps were reduced to 0.0415 mm and 0.0381 mm respectively, which were half of their original space size. These space steps did not exceed the space limit of $2\Delta x > \Delta y$ and Δz , also, $\Delta < \lambda/10$. The simulated results of the old and new space steps are presented Figure 4.8.



(a)



(b)

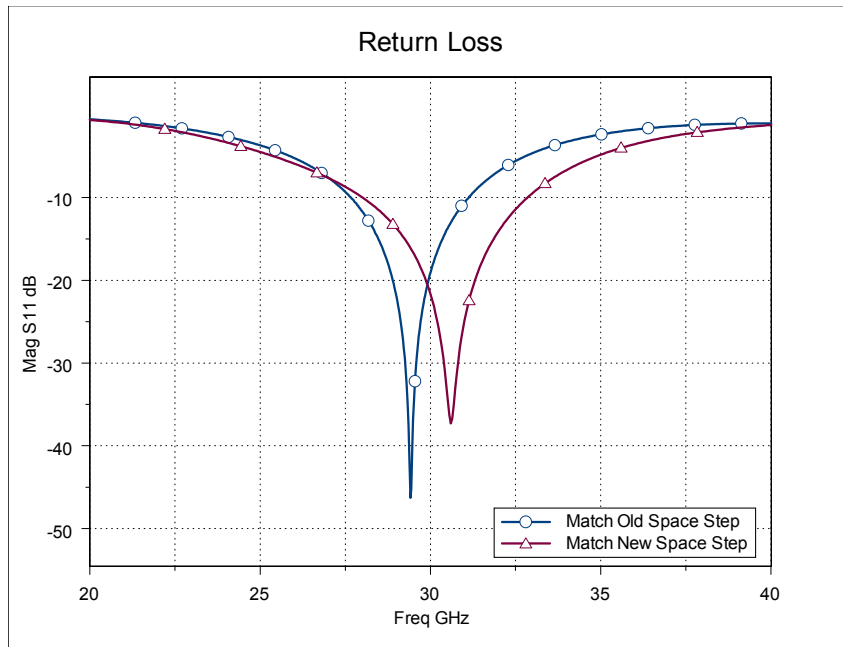
Figure 4.8. AFSA simulated results at old and new space steps. (a) Return Loss. (b) Input Impedance.

At this new space steps the antenna resonant matching frequency increased from 29.38 to 29.8 GHz, its reflections increased from -45 to -12 dB and the bandwidth changed from 3.5 to 3.2 GHz. These results demonstrated that the original space steps chosen were not adequate for simulating the weighted average equation. Additional simulations were conducted by reducing the new space steps by half and no significant change in the responses was observed. Therefore, the antenna at the new space steps of $\Delta x=0.0415$, $\Delta y=0.0625$ and $\Delta z=0.0381$, all dimensions in mm, was matched and its results studied. Table 4.4 presents the new dimensions for the design parameters matching at the new space steps.

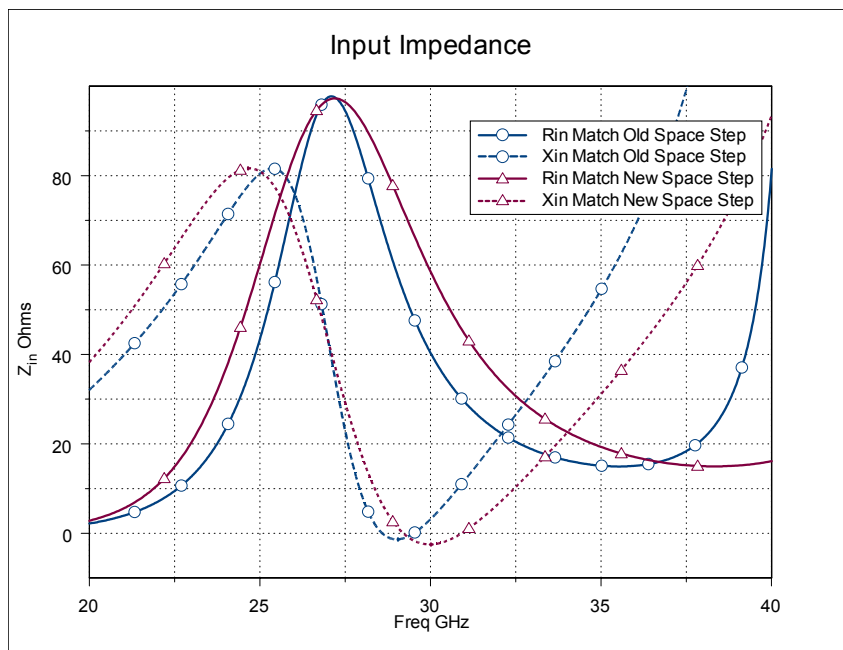
Table 4.4
AFSA Matching Dimensions at New Space Step

Parameters	Dimension (mm)
L	5.068
L1	2.034
W1	0.437
W2	0.166
W3	0.125
S	0.3125
Lf	0.1875
Wf	0.083
Sf	0.2905

Note that the only dimensions that varied were the top slot length ($L1$) and width ($W1$). As mentioned before, an increase in this width causes a shift in the resonant frequency. The separation between the transmission lines was varied in order to accommodate par unit cells for that dimension. Figure 4.9 presents the output responses for the matched antennas at the old and the new space steps.

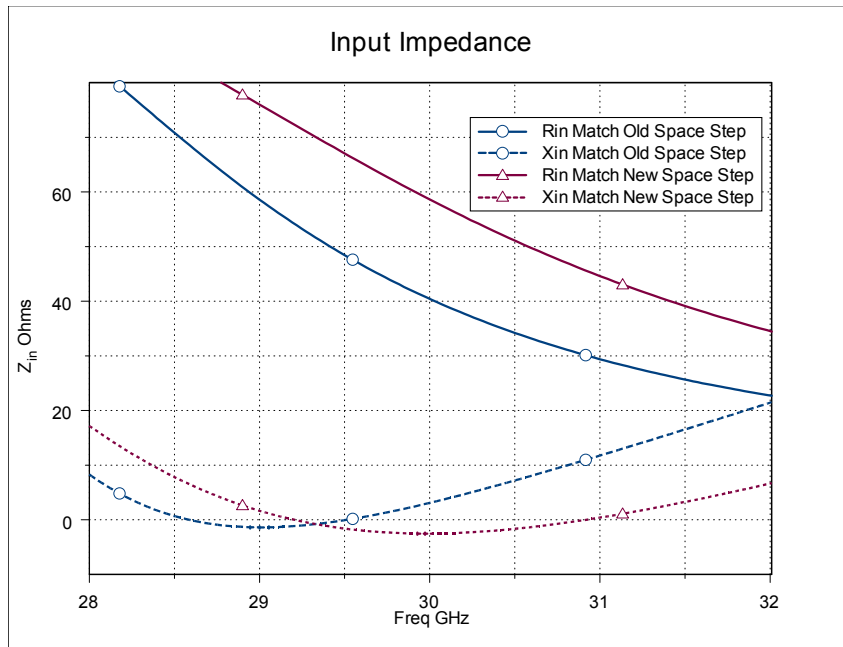


(a)

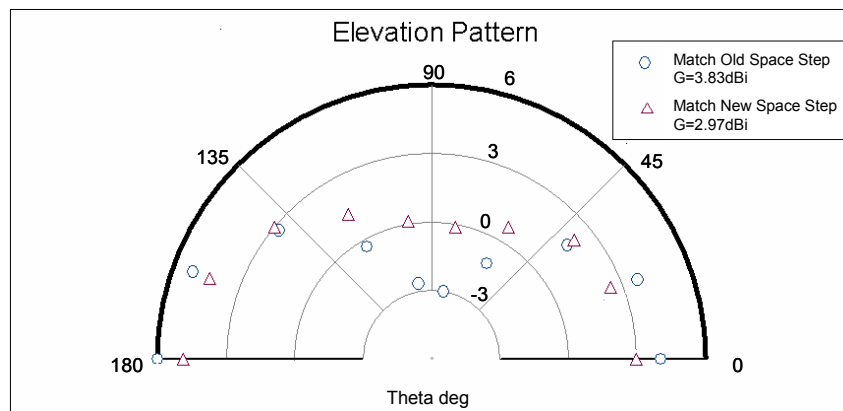


(b)

Figure 4.9. Matched AFSA simulated results at old and new space steps. (a) Return Loss. (b) Input Impedance. (c) Input Impedance at zoomed frequency range. (d) Elevation Pattern.



(c)



(d)

Figure 4.9. Continued

This AFSA with a more reduced space step reached good resonant matching frequency, reflections and gain, as well as, better bandwidth and dual resonance. Comparing the simulated results between the previous matched AFSA with the current matched AFSA it was found that the resonant matching

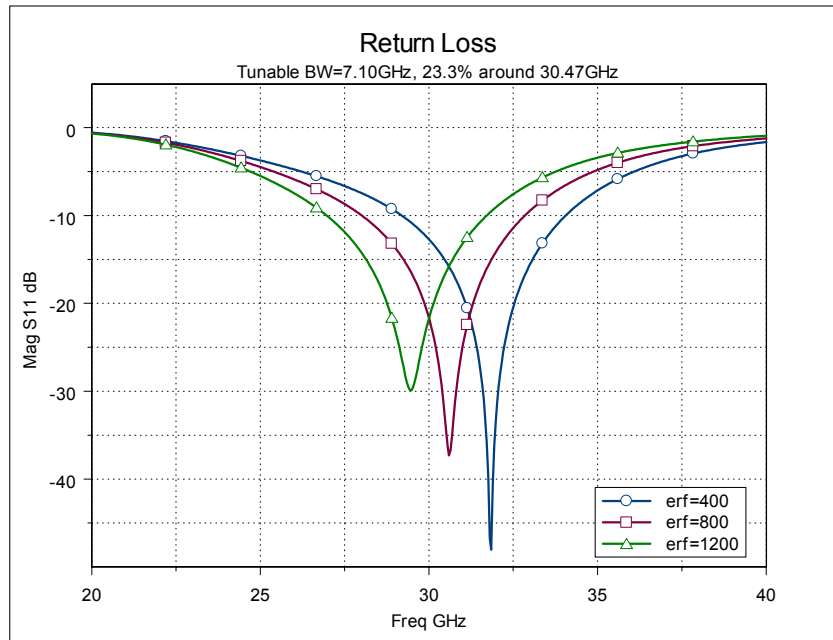
frequency changed by approximately 1 GHz from 29.38 to 30.47 GHz, the reflections and bandwidth increased from -45 to -37 dB and from 3.5 to 4.85 GHz respectively and the gain decreased from 3.83 to 2.97 dBi. These results are within the desired goals.

The dual resonance varied by approximately 1 GHz reflecting an input resistance change of approximately 3 ohms. The previous matched AFSA presented dual resonance at 28.55 and 29.46 GHz for an input resistance range between 48.57 and 68.54 ohms while the current matched AFSA dual resonance occurred at 29.13 and 30.82 GHz yielding an input resistance range between 45.70 and 72.18 ohms. Note that compact input resistance ranges were found at these dual resonance frequencies.

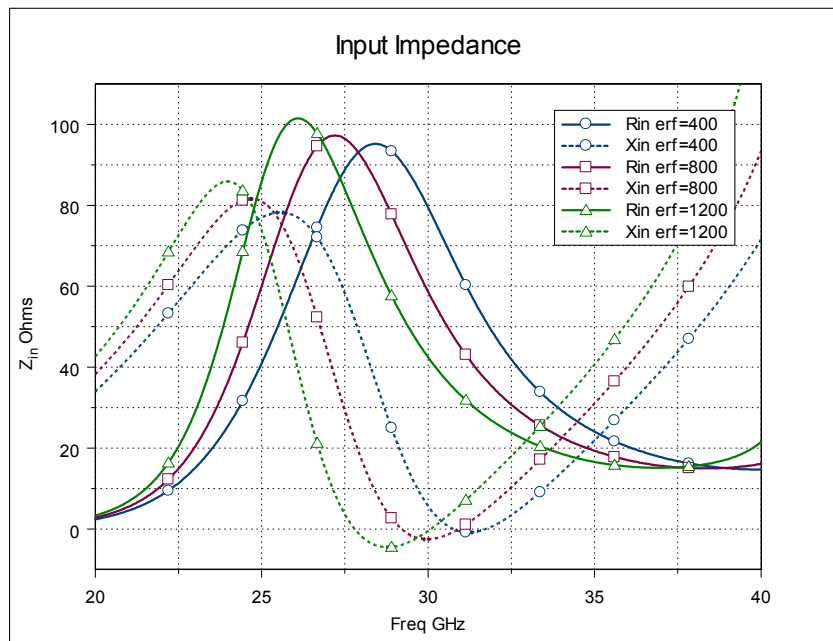
These results show that the new space steps chosen were adequate for simulating the weighted average equation. The dimensions obtained do agree with the desired goals, therefore, this AFSA was referred to as the Folded Slot Antenna (FSA) and its matching dimensions were referred to as the design dimensions. The overall structure was called the CPW-fed FSA.

4.4 Thin Film Relative Permittivity Variation

After the design dimensions were accomplished, the thin film relative permittivity was varied and its effect on the output responses studied. It was desired to explore the behavior of such antenna as demonstrated below.

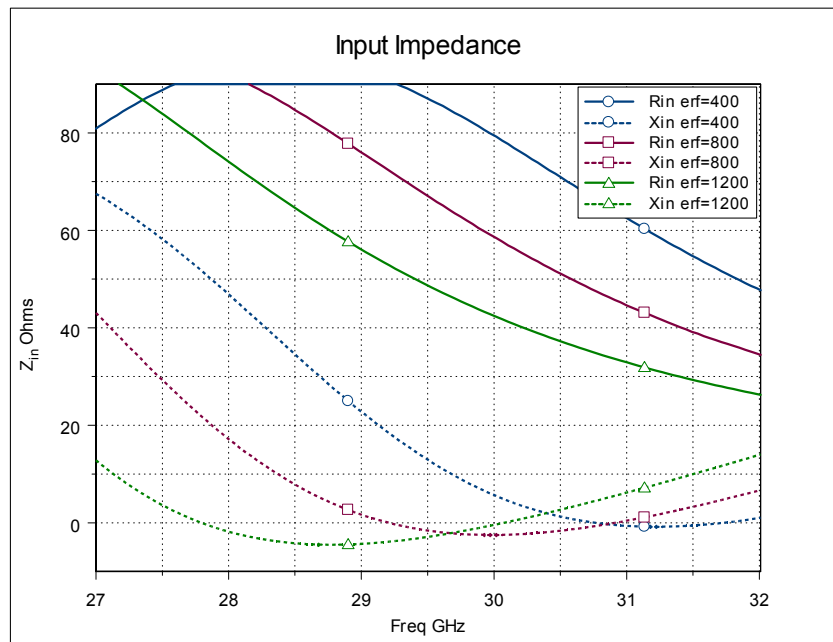


(a)

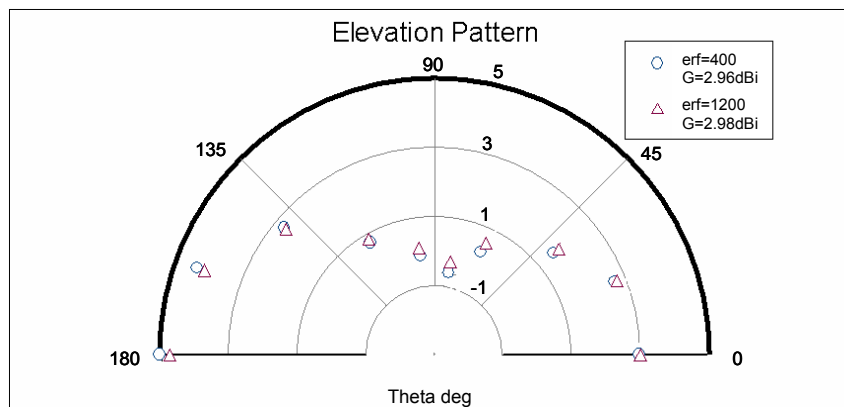


(b)

Figure 4.10. CPW-fed FSA simulated results at varied film relative permittivity. (a) Return Loss. (b) Input Impedance. (c) Input Impedance at zoomed frequency range. (d) Elevation Pattern.



(c)



(d)

Figure 4.10. Continued

From the return loss plot we could appreciate the tuning that was achieved by varying the relative permittivity of the thin film. Note that the reflections varied from -50 to 0 dB for a frequency range from 20 to 40 GHz. The lowest reflections for the FSA occurred at 29.31

GHz for a relative permittivity of 1200, 30.47 GHz for a relative permittivity of 800 and 31.72 GHz for a relative permittivity of 400 with a VSWR < 2 and tunable bandwidth of 7.10 GHz for 23.33% around 30.47 GHz. A decrease in the relative permittivity of the thin film caused the reflections to decrease and the frequency to increase by 1 GHz. This behavior occurs because the fields tend to concentrate more in the substrate.

In the input impedance plots, the resistance varied from 4 to 100 ohms and the reactance varied from -5 to 90 ohms for a frequency range from 20 to 40 GHz. The effect the variation in the relative permittivity of the thin film had on the input impedance is the same as the effect it had on the reflections. The impedance decreased as the relative permittivity of the thin film decreased but the frequency increased.

The zoomed input impedance plot, Figure 4.10 c, shows where the dual resonance occurred at a frequency range from 27 to 32 GHz. Note that the dual resonant frequencies occurred at 27.7 and 30 GHz for $\epsilon_{rf} = 1200$, at 29.1 and 30.8 GHz and for $\epsilon_{rf} = 800$ and at 30.7 and 31.7 GHz for $\epsilon_{rf} = 400$. These dual resonant frequencies yield a total frequency shift of 4 GHz at the resonant frequency range between 27.7 GHz and 31.7 GHz. At this resonant frequency range dual input resistances of 78.35 and 49.81 ohms were obtained at the resonant frequencies of 27.7 and 31.7 GHz respectively resulting in a total resistance shift of 28.54 ohms.

This structure had a gain between 2.96 dBi for a relative permittivity of 400 and 2.98 dBi for a relative permittivity of 1200. The elevation pattern seemed almost not affected by the change in permittivity. Generally the gain of a slot antenna is about 1.6 dBi and this FSA was approximately 3 dBi.

4.5 Design of Experiment

Now that is clear what the effects the BSTO film had on the output responses, it was pertinent to find the optimum design dimensions for this CPW-fed FSA to comply with the desired design specifications. A technique called Design of Experiment (DoE) was used to have an idea of the number of simulations it required to achieve dual resonance and maximize the obtained results information. The DoE input factors were tabulated in Table 4.5.

Table 4.5
DoE Input Factors

Parameter	Low Level (-1) Dimension (mm)	Center Level (0) Dimension (mm)	High Level (1) Dimension (mm)
S	0.25	0.3125	0.375
W1	0.3745	0.437	0.4995
W2	0.1035	0.166	0.2285
W3	0.10	0.125	0.1875
ϵ_{rf}	400	800	1200

With these 5 input factors a geometrical design of $2^4 3^1$ combinations were obtained for a total of 48 combinations as shown in Table 4.6. The ϵ_{rf} varied at all three levels the remaining input factors varied at the low and high levels. The simulated output responses for these design combinations were shown in Figure 4.11 and 4.12 through Bull's Eye.

Table 4.6
DoE Geometrical Design Combinations

Design	S (mm)	W1 (mm)	W2 (mm)	W3 (mm)	ϵ_{rf}
1a	0.25	0.3745	0.1035	0.10	400
2a	0.25	0.3745	0.2285	0.10	400
3a	0.25	0.4995	0.1035	0.10	400
4a	0.25	0.4995	0.2285	0.10	400

Table 4.6
DoE Geometrical Design Combinations (Continued)

Design	S (mm)	W1 (mm)	W2 (mm)	W3 (mm)	ϵ_{rf}
5a	0.375	0.3745	0.1035	0.10	400
6a	0.375	0.3745	0.2285	0.10	400
7a	0.375	0.4995	0.1035	0.10	400
8a	0.375	0.4995	0.2285	0.10	400
9a	0.25	0.3745	0.1035	0.1875	400
10a	0.25	0.3745	0.2285	0.1875	400
11a	0.25	0.4995	0.1035	0.1875	400
12a	0.25	0.4995	0.2285	0.1875	400
13a	0.375	0.3745	0.1035	0.1875	400
14a	0.375	0.3745	0.2285	0.1875	400
15a	0.375	0.4995	0.1035	0.1875	400
16a	0.375	0.4995	0.2285	0.1875	400
1b	0.25	0.3745	0.1035	0.10	800
2b	0.25	0.3745	0.2285	0.10	800
3b	0.25	0.4995	0.1035	0.10	800
4b	0.25	0.4995	0.2285	0.10	800
5b	0.375	0.3745	0.1035	0.10	800
6b	0.375	0.3745	0.2285	0.10	800
7b	0.375	0.4995	0.1035	0.10	800
8b	0.375	0.4995	0.2285	0.10	800
9b	0.25	0.3745	0.1035	0.1875	800
10b	0.25	0.3745	0.2285	0.1875	800
11b	0.25	0.4995	0.1035	0.1875	800
12b	0.25	0.4995	0.2285	0.1875	800
13b	0.375	0.3745	0.1035	0.1875	800
14b	0.375	0.3745	0.2285	0.1875	800
15b	0.375	0.4995	0.1035	0.1875	800
16b	0.375	0.4995	0.2285	0.1875	800
1c	0.25	0.3745	0.1035	0.10	1200
2c	0.25	0.3745	0.2285	0.10	1200
3c	0.25	0.4995	0.1035	0.10	1200
4c	0.25	0.4995	0.2285	0.10	1200
5c	0.375	0.3745	0.1035	0.10	1200
6c	0.375	0.3745	0.2285	0.10	1200
7c	0.375	0.4995	0.1035	0.10	1200
8c	0.375	0.4995	0.2285	0.10	1200
9c	0.25	0.3745	0.1035	0.1875	1200
10c	0.25	0.3745	0.2285	0.1875	1200
11c	0.25	0.4995	0.1035	0.1875	1200
12c	0.25	0.4995	0.2285	0.1875	1200
13c	0.375	0.3745	0.1035	0.1875	1200
14c	0.375	0.3745	0.2285	0.1875	1200
15c	0.375	0.4995	0.1035	0.1875	1200
16c	0.375	0.4995	0.2285	0.1875	1200

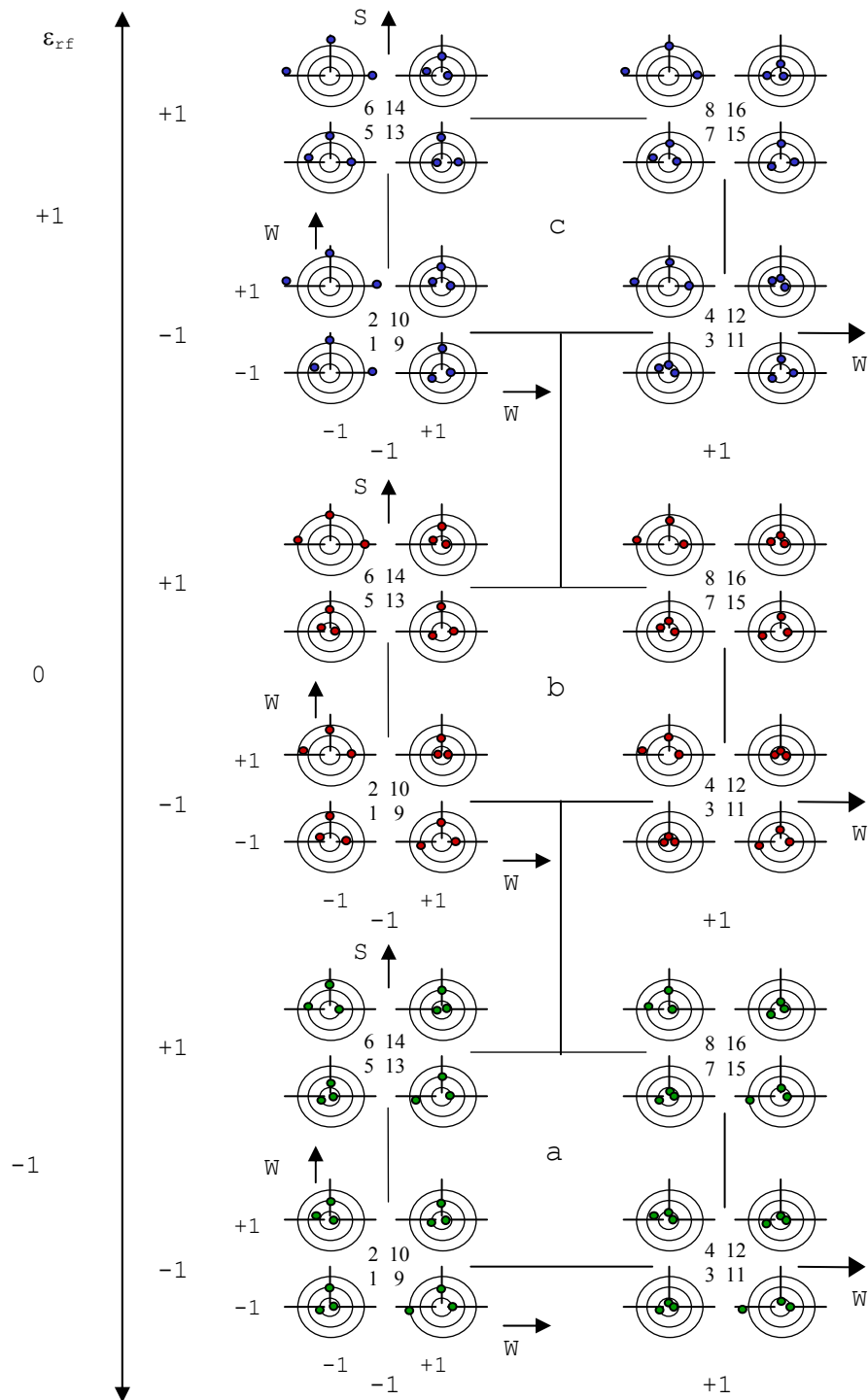


Figure 4.11. DoE graphical visualization with Bull's Eye representation of the goal responses simulated at the respective input factors.

Note from Figure 4.11 that as the thin film relative permittivity increased the matching resonant frequency decreased by 1 GHz, the reflections increased approximately 2 dB to 4 dB and the bandwidth decreased approximately 0.1 GHz to 1.2 GHz for each DoE design. The tunable bandwidth obtained from the DoE designs was approximately 14% to 22% around their matching resonant frequencies.

The designs that provided matching resonant frequency at Ka-band with minimum reflections ($S_{11} < -20$ dB) throughout the varied thin film relative permittivity were Design 3 and 12. These designs consisted of a tunable FSA with its top slot width ($W1$) at its high level dimension and its separation between the top and bottom slots (S) at its low level dimension with its side ($W2$) and bottom slot ($W3$) widths at their low or high level dimension.

The designs that provided wide ($BW > 3$ GHz) and tunable ($TBW > 18\%$) bandwidth throughout the varied thin film relative permittivity were Design 3, 7, 10, 12, 14, and 16. The DoE input factor combination that yielded these designs were $W1$ at its high level dimension, S at its low or high level dimension and $W2$ and $W3$ at their low level dimension, or, $W1$ and S at their low or high level dimension in combination with $W2$ and $W3$ at their high level dimension.

The results indicate that the designs that complied with the desired goal responses of matching resonant frequency at Ka-band with minimum reflections and wide bandwidth throughout the varied thin film relative permittivity were Design 3 and 12.

Figure 4.12 demonstrates the geometrical representation of DoE input factors with Bull's Eye representation of the simulated dual resonance behavior.

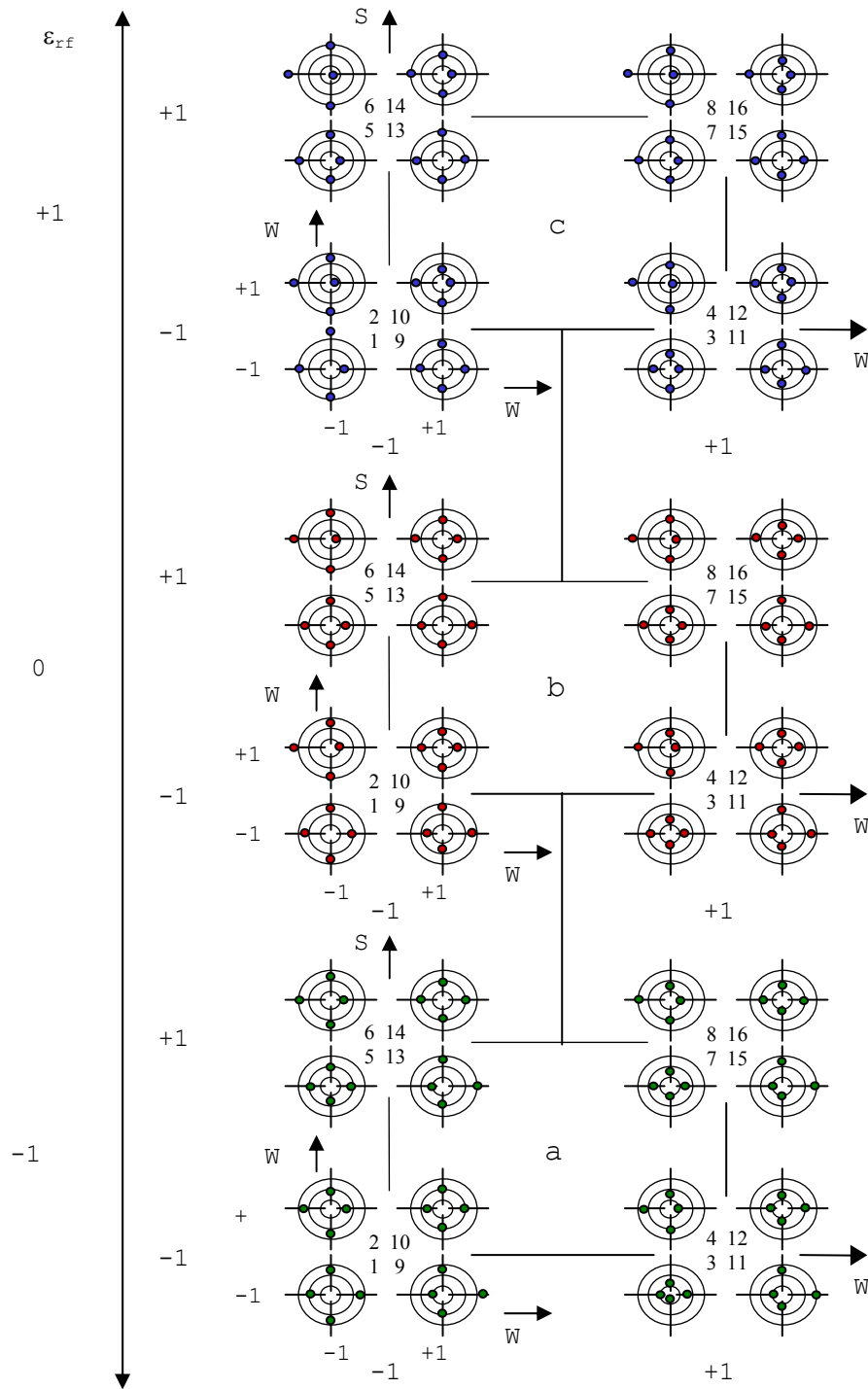


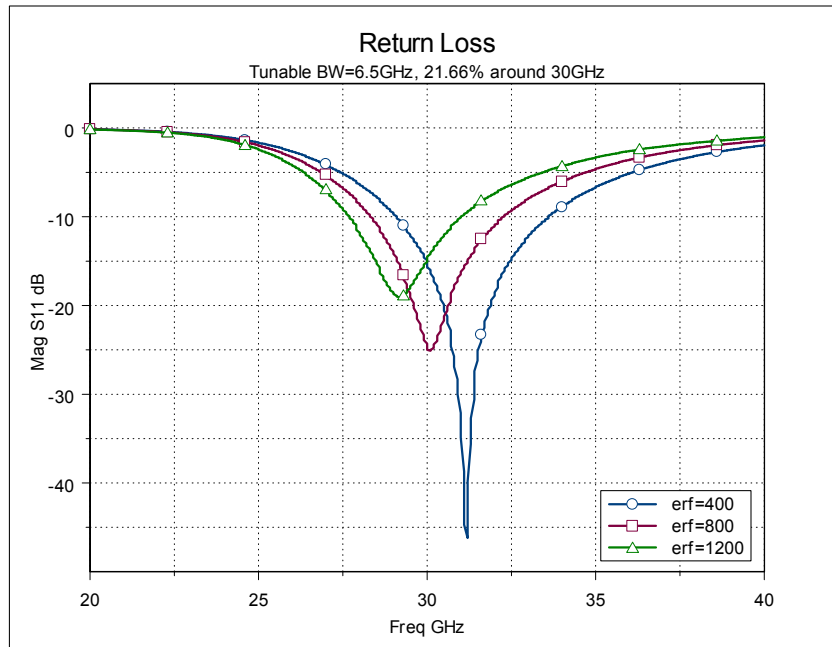
Figure 4.12. DoE graphical visualization with Bull's Eye representation of the dual resonance behavior simulated at the respective input factors.

Note from Figure 4.12 that as the relative permittivity increased the resonant frequencies decreased by 1 GHz, the first resonant input resistance increased by 20 ohms and the second resonant input resistance decreased by 3 ohms for each DoE design. Therefore a noticeable effect on the second resonant input resistance occurred with relative permittivity increase.

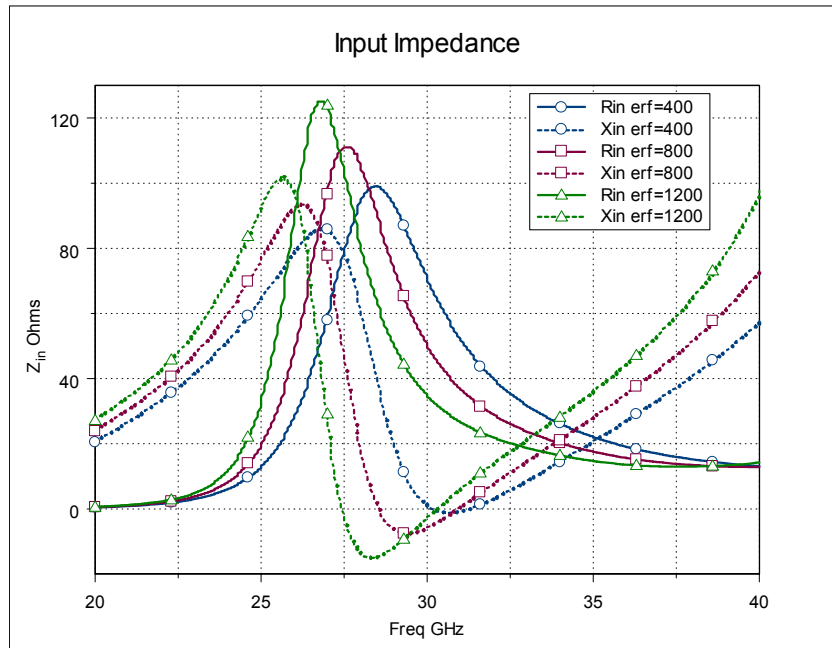
A compact input impedance loop around 50 ohms can be achieved by choosing a low first resonant input resistance, R_1 , (between 70 and 100 ohms) and a high second resonant input resistance, R_2 , (between 28 and 48 ohms). R_1 was observed with S at its low or high level dimension, $W1$ at its high level dimension with $W2$ and $W3$ at their low level dimension. R_1 can be also obtained with S at its low level dimension with $W1$ and $W2$ at their high level dimension in combination with $W3$ at its low or high level dimension. Note that R_2 occurred with S at its low level dimension, $W1$ at its high level dimension in combination with $W2$ and $W3$ at their low or high level dimension. This resonance also occurred with S and $W1$ at their high level dimension with $W2$ at its low level dimension and $W3$ at its low or high level dimension, or with S , $W1$, and $W3$ at their high level dimensions.

The dual resonance behavior that occurred between Design 3 and 12, at the ϵ_{rf} low, center and high level dimensions was an increase of 35 and 14 ohms and a decrease of 4 ohms respectively for R_1 . A decrease of 12 and 2 and an increase of 2 ohms were observed for R_2 .

Figures 4.13 and 4.14 studied with more detail the simulated results of these designs at the three thin film relative permittivities.

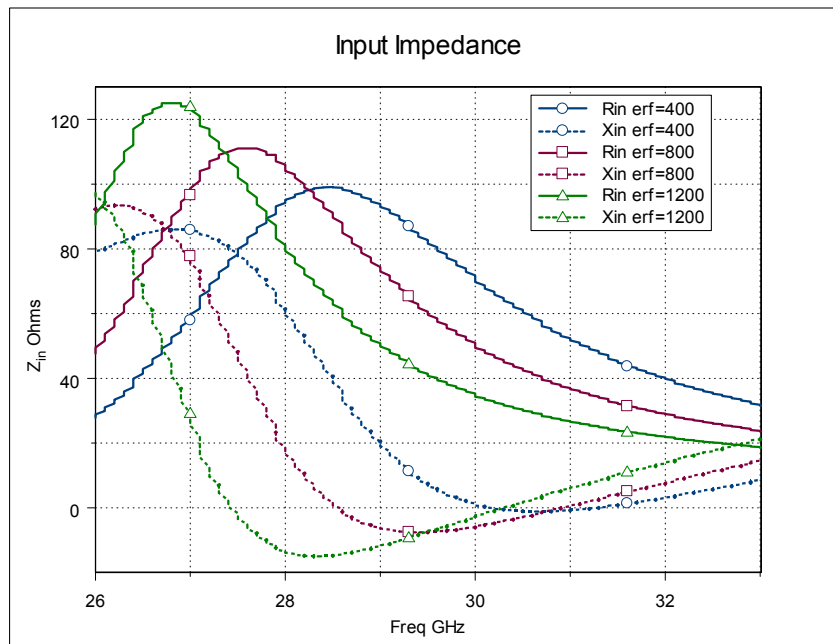


(a)

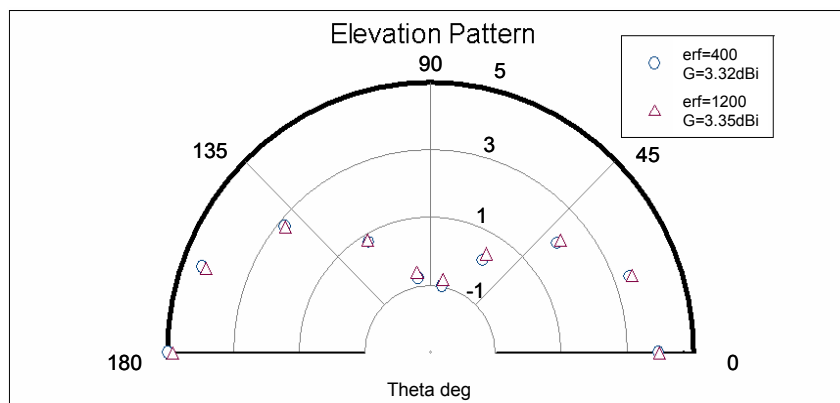


(b)

Figure 4.13. Design 3 simulated results at varied film relative permittivity. (a) Return Loss. (b) Input Impedance. (c) Input Impedance at zoomed frequency range. (d) Elevation Pattern.



(c)



(d)

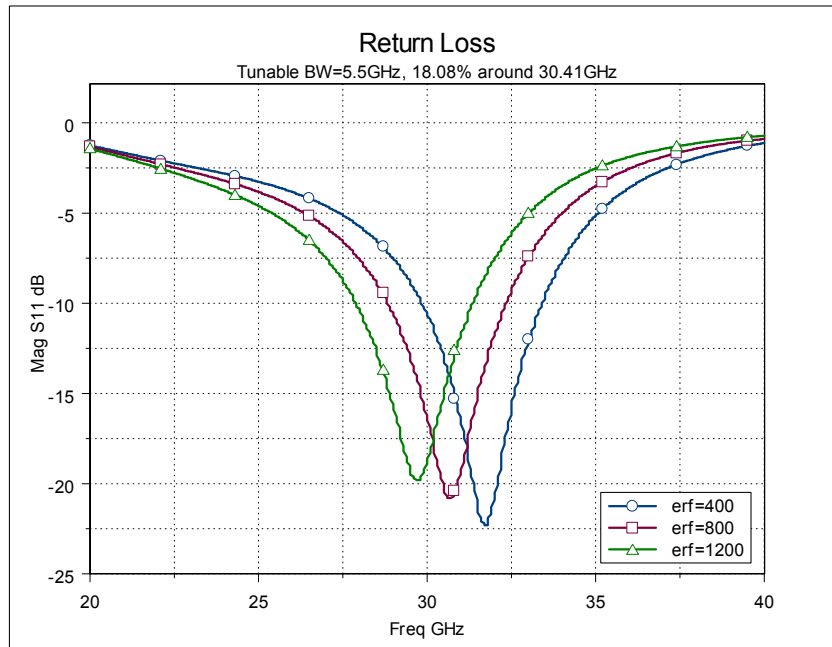
Figure 4.13. Continued

The previous results of a tunable FSA with its separation between the top and bottom slots (S), top ($W1$), side ($W2$) and bottom ($W3$) slot widths at their low level dimensions had reflections varied from -50 to 0 dB for a frequency range from 20 to 40 GHz. The lowest reflections

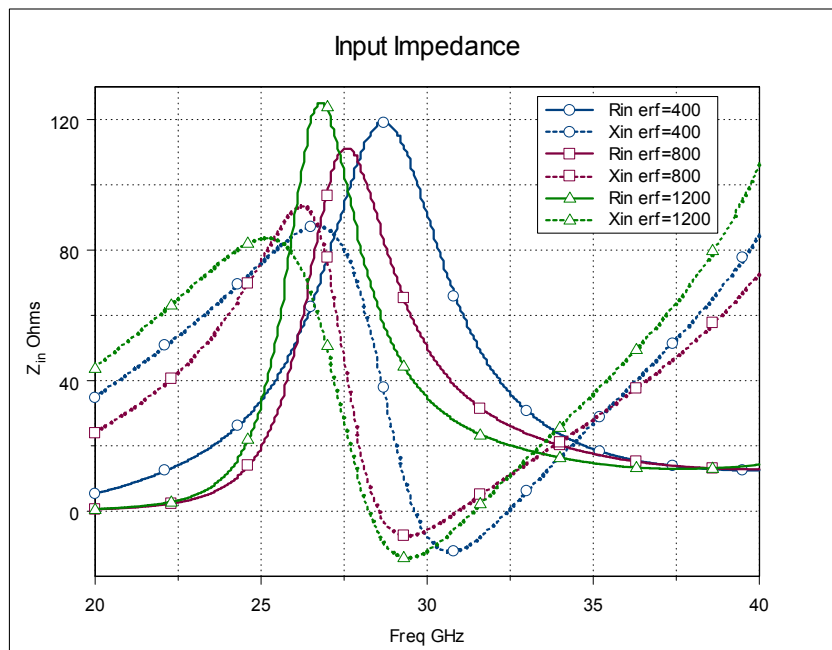
for the FSA occurred at 28.96 GHz for a relative permittivity of 1200, 30 GHz for a relative permittivity of 800 and 31.12 GHz for a relative permittivity of 400 with a tunable bandwidth of 6.5 GHz for 21.66% around 30 GHz.

In the input impedance plots, the resistance varied from 0 to 130 ohms and the reactance varied from -20 to 100 ohms for a frequency range from 20 to 40 GHz. The dual resonance occurred at the frequency range from 26 to 33 GHz as shown in Figure 4.13 c. Note that the dual resonant frequencies occurred at 27.4 and 30.3 GHz, 28.5 and 30.9 GHz and 30.1 and 31.3 GHz, for the respective thin film relative permittivity of 1200, 800 and 400. A total frequency shift of 3.9 GHz at the resonant frequency range between 27.4 GHz and 31.3 GHz was observed. At this resonant frequency range dual input resistances obtained at the relative permittivities of 1200, 800 and 400 were 106.83 and 31.60, 88.01 and 37.50, and, 67.72 and 48.37 respectively resulting in a total resistance shift of 58.46 ohms. The individual resistance shift from one ϵ_{rf} level dimension to the other (1200-800, 800-400) for the first resonant input resistance was 20 ohms and for the second resonant input resistance were 5 and 11 (mainly because of the reflections) ohms. Therefore, a tunable FSA with S , $W1$, $W2$ and $W3$ at their low level dimensions had a noticeable effect on the first resonant input resistance. The input impedance loop tends to expand to the right.

This structure had a gain between 3.32 dBi for a relative permittivity of 400 and 3.35 dBi for a relative permittivity of 1200. This gain exceeds the gain of a slot antenna which is generally 1.6 dBi.

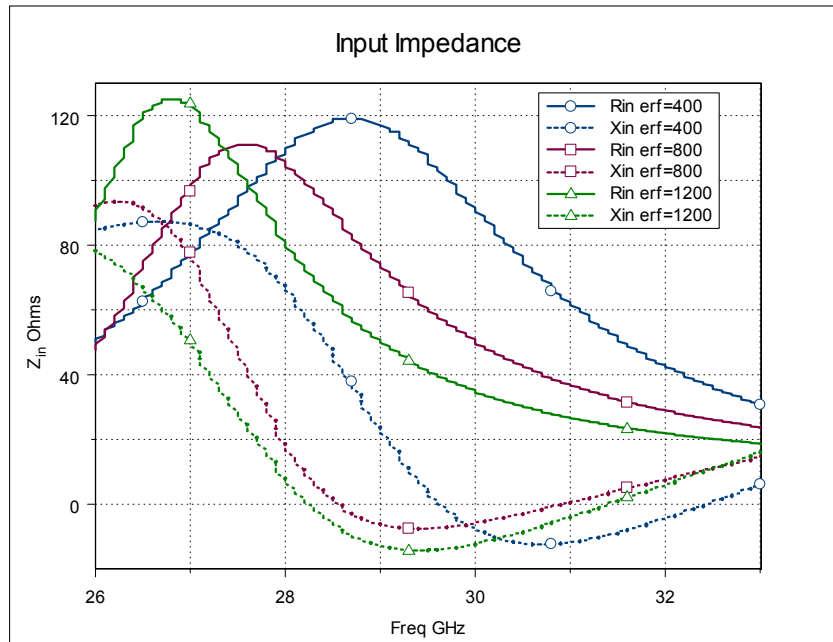


(a)

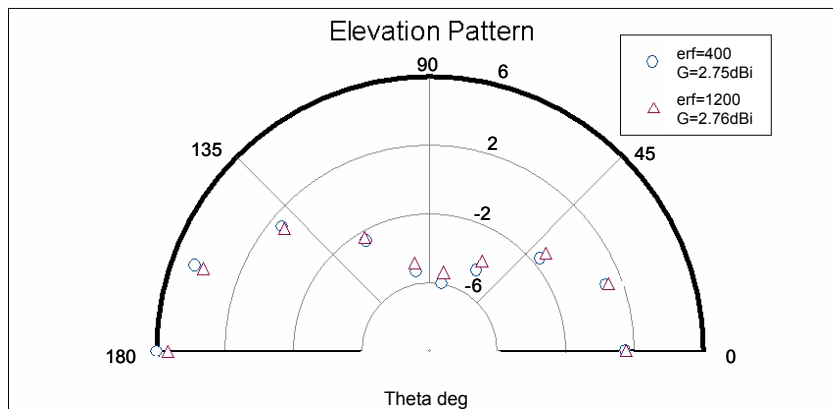


(b)

Figure 4.14. Design 12 simulated results at varied film relative permittivity. (a) Return Loss. (b) Input Impedance. (c) Input Impedance at zoomed frequency range. (d) Elevation Pattern.



(c)



(d)

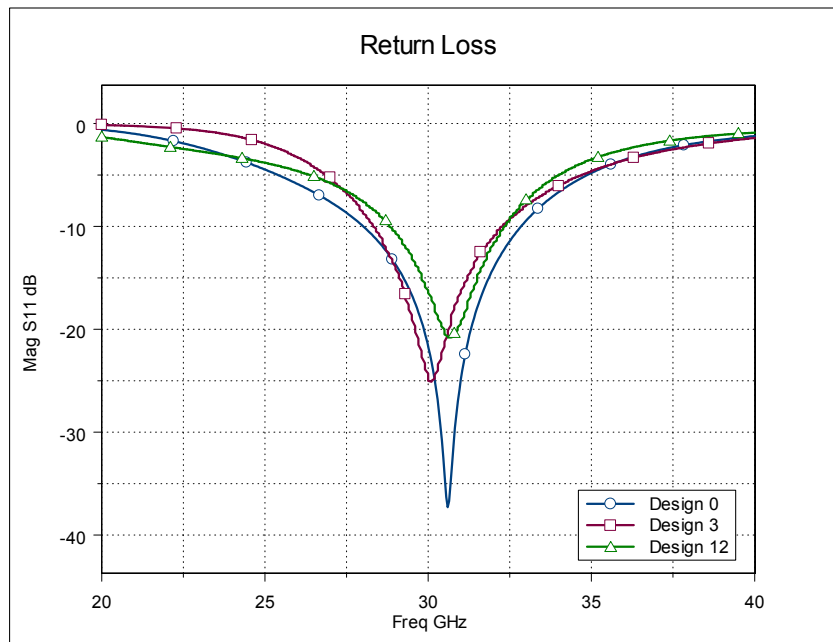
Figure 4.14. Continued

These simulated results of a tunable FSA with its separation between the top and bottom slots (S) and top slot width ($W1$) at their low level dimensions and with its side ($W2$) and bottom ($W3$) slot widths at their high level dimensions yielded reflections varied from -2 to 0 dB for a

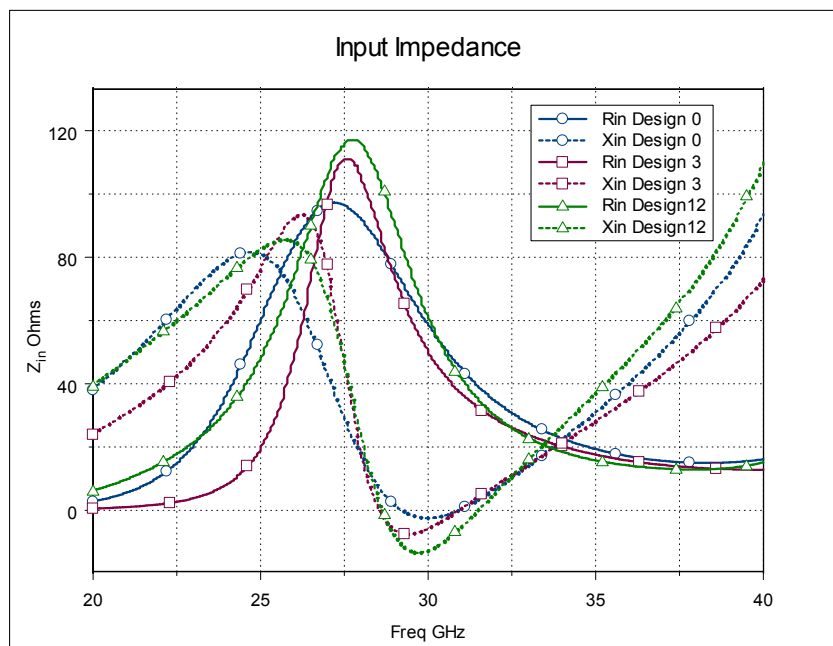
frequency range from 20 to 40 GHz. The lowest reflections for the FSA occurred at 29.41, 30.41 and 31.46 GHz for the respective relative permittivity of 1200, 800 and 400. A tunable bandwidth of 5.5 GHz for 18.08% around 30.41 GHz was experienced.

The resulting input resistances varied from -20 to 120 ohms through a frequency range from 20 to 40 GHz. The FSA dual resonant frequencies occurred at 27.59 and 30.55 GHz for a relative permittivity of 1200, at 28.54 and 31.42 GHz for 800 and at 29.54 and 32.37 GHz for 400. This resonance resulted in a total frequency shift of 4.78 GHz at the resonant frequency range between 27.59 GHz and 32.37 GHz. Dual input resistances were obtained at 102.41 and 33.46, 102.40 and 34.52, and, 102.44 and 36.56 for relative permittivities of 1200, 800 and 400 respectively, which resulted in a total resistance shift of 68.98 ohms. The individual resistance shift from one ϵ_{rf} level dimension to the other (1200-800, 800-400) for the first and second resonant input resistances were approximately 0 ohms and 1.05 ohms. Therefore the tunable FSA with S and $W1$ at their low level dimensions and $W2$ and $W3$ at their high level dimensions had an effect on the second resonant input resistance. The input impedance loop tends to expand to the left. This structures gain of approximately 2.76 dBi exceeded the general gain of a slot antenna.

In Figure 4.15 the Design 3 and 12 were compared with the CPW-fed FSA (Design 0) used to develop the geometrical design at the thin film relative permittivity center level dimension.

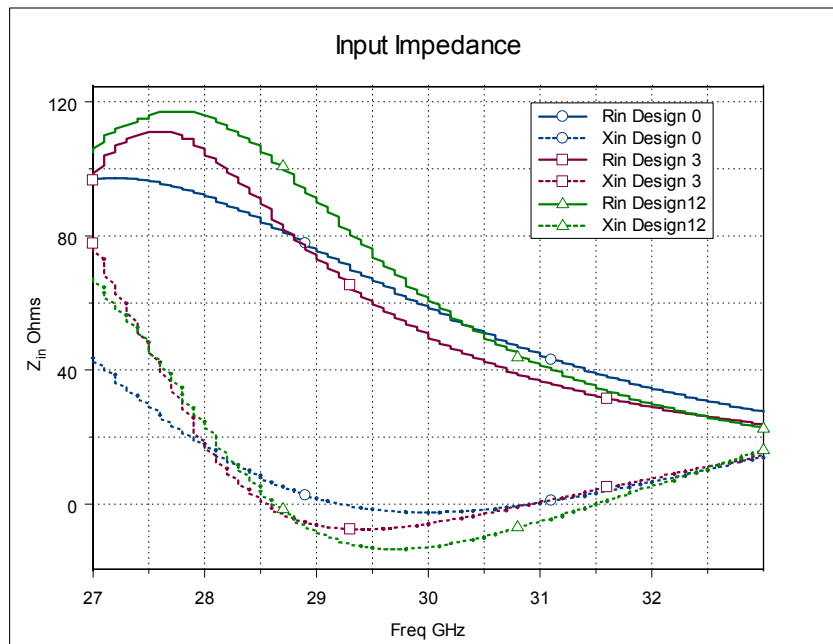


(a)

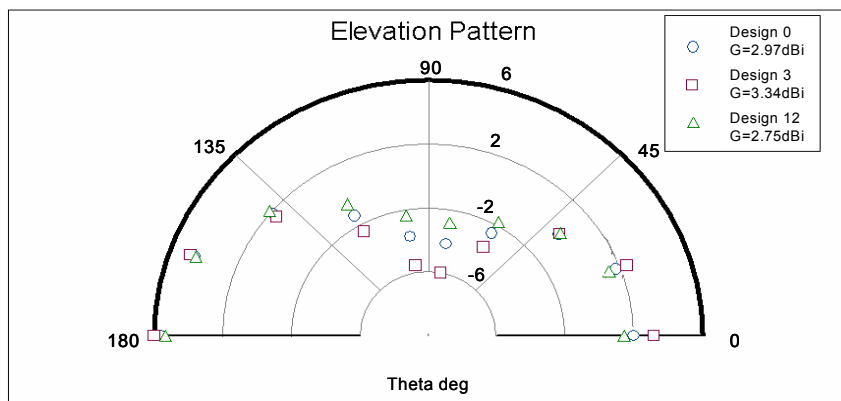


(b)

Figure 4.15. Optimum designs at film relative permittivity of 800. (a) Return Loss. (b) Input Impedance. (c) Input Impedance at zoomed frequency range. (d) Elevation Pattern.



(c)



(d)

Figure 4.15. Continued

As shown in the return loss plot, the reflections varied from -40 to -10 dB for a frequency range from 20 to 40 GHz. Design 12 and the Design 0 resonated at the same frequency of 30.4 GHz although with different reflections, Design 3 resonated at 30 GHz. Design 3 and Design 12 had

bandwidths of 3.9 and 3.5 GHz respectively which were approximately 1.35 GHz smaller than Design 0. The chosen designs complied with the desired goals of matching resonant frequency at 30 GHz, minimum reflections ($S_{11} < -20$) and bandwidth greater than 3 GHz.

In the input impedance plots, the resistance varied from 0 to 120 ohms and the reactance varied from -20 to 100 ohms for a frequency range from 20 to 40 GHz. The zoomed input impedance plot, Figure 4.15 c, shows where the dual resonance occurred at a frequency range from 27 to 33 GHz. Note that the dual resonant frequencies for Design 0 occurred at 29.13 and 30.82 GHz for Design 3 at 28.54 and 30.93 GHz and for Design 12 at 28.54 and 31.42 GHz. A dual resonance frequency shift of approximately 1 GHz at the resonant frequency range between 29 GHz and 31 GHz was observed. At this resonant frequency range dual resonant resistances of 72.18 and 45.70 ohms, 88.01 and 37.50 ohms, and, 102.40 and 34.52 were obtained for the Designs 0, 3 and 12 respectively. Comparing the dual resonant resistances of Design 3 and 12 with Design 0 it was observed that an increase of 16 and 14 ohms at the first resonant frequency and a decrease of 8 and 3 ohms at the second resonant frequency took place resulting in wider input impedance range.

The gain of Design 3 increased 0.37 dBi and Design 12 decreased 0.22 dBi in comparison with Design 0. Therefore if more gain is desired a tunable FSA with S , $W1$, $W2$ and $W3$ at their low level dimensions is appropriate.

4.6 Goal-model Development

The goal-models from the desired output responses were generated by Design Expert. These models were obtained from the prediction equations generated through ANOVA. The following output response models consisted of the most significant coded factors. The model that predicts the matching resonant frequency is given by,

$$\begin{aligned} \text{Fr50} = & 29.72 - 0.27*A + 0.13*B - 1.04*C + 1.21*D + 1.10*E[1] \\ & - 0.039*E[2] + 0.12*CD - 0.076*CE[1] + 4.583E-3*CE[2] \end{aligned} \quad (4.1)$$

The model that predicts minimum reflections is given by,

$$\begin{aligned} S_{11} = & 16.61 + 0.88*A - 3.04*B + 1.09*C - 3.08*E[1] + 0.58* \\ & E[2] + 0.97*AB + 0.99*BCE[1] + 0.83*BD - 1.32*BE[1] + \\ & 0.38*BE[2] - 2.03*CD + 1.09*CE[1] - 0.31*CE[2] + 1.75* \\ & DE[1] - 0.39*DE[2] - 0.66*ABC - 0.65*ABD - 1.18*BCD + \\ & 0.89*BCE[1] - 0.28*BCE[2] + 1.00*BDE[1] - 0.35*BDE[2] \\ & - 0.97*CDE[1] + 0.36*CDE[2] + 0.69*ABCD - 1.02* \\ & BCDE[1] + 0.35*BCDE[2] \end{aligned} \quad (4.2)$$

The model that predicts bandwidth is given by,

$$\begin{aligned} \text{BW} = & 2.98 + 0.39*B - 0.14*C + 0.22*D + 0.61*E[1] + 0.021* \\ & E[2] - 0.23*BD - 0.19*BE[1] - 0.017*BE[2] + 0.43*CD - \\ & 0.51*DE[1] - 0.021*DE[2] + 0.10*ABC + 0.10*ABD + 0.15* \\ & ACD + 0.16*BDE[1] + 0.058*BDE[2] - 0.067*ABDE[1] - \\ & 0.079*ABDE[2] \end{aligned} \quad (4.3)$$

The model that predicts the first resonant frequency is given by,

$$\begin{aligned} \text{Fr1} = & 27.54 - 0.35*A + 0.35*B - 0.78*C + 0.94*D + 0.91*E[1] \\ & + 0.016*E[2] \end{aligned} \quad (4.4)$$

The model that predicts the first resonant input resistance is given by,

$$R1 = 135.05 + 5.46*A - 15.22*B - 9.15*C + 3.25*D - 10.20*E[1] - 1.29*E[2] + 3.84*AB + 3.13*AC + 6.82*BD - 14.23*CD + 10.22*DE[1] + 1.56*DE[2] - 3.81*ABC - 4.15*ACD + 3.69*ABCD \quad (4.6)$$

The model that predicts the second resonant frequency is given by,

$$Fr2 = 31.44 - 0.20*A - 0.27*B - 0.89*C + 0.87*D + 0.88*E[1] - 0.014*E[2] + 0.17*BD \quad (4.7)$$

The model that predicts the second resonant input resistance is given by,

$$R2 = 29.41 + 3.50*B - 2.11*C + 2.51*D + 3.28*E[1] - 0.24*E[2] - 0.76*AB - 0.95*BC + 1.87*CD - 1.40*DE[1] + 0.15*DE[2] + 1.04*BCD \quad (4.8)$$

Every model was linear and the letters A, B, C, D and E were the codified factors that represented the input factors. These codified factors were replaced in the modeled equations with coded coefficients between -1 and +1, depending on the design dimension. The separation between the top and bottom slot widths (S) and the top ($W1$), side ($W2$) and bottom ($W3$) slot widths were represented by the letters A, B, C and D respectively. The thin film relative permittivity (ϵ_{rf}) was represented with the letter E. Since this factor was a multilevel categorical factor, the first coefficient was the difference of level 1 from the overall average; the second coefficient was the difference of level 2 from the overall average. The negative sum of all the coefficients was the difference of the last level from the

overall average. The following table presents the mentioned relative permittivity coded coefficients.

Table 4.7
Relative Permittivity Coded Coefficients

ϵ_{rf}	E[1]	E[2]
400	1	0
800	0	1
1200	-1	-1

After these models were retrieved they were tested by substituting the codified coefficients from a new CPW-fed FSA design in the equations for validation purposes. The codified values used were the designs that represented the middle point of the right small squares in Figure 3.3. In these designs the input factor S had low and high values, the input factor $W1$ had low values, $W2$ and $W3$ had center and intermediate values respectively and ϵ_{rf} had low, center and high values. The following tables present the coded coefficients and design dimensions used to validate the model equations. The dimensions of the structure length and CPW feed were not changed and were presented in Table 4.4.

Table 4.8
Validation Design Dimensions

Parameter	Design 17		Design 19	
	Dimension	Coded	Dimension	Coded
S	0.25	-1	0.3745	1
W1	0.3745	-1	0.3745	-1
W2	0.166	0	0.166	0
W3	0.125	-0.428	0.125	-0.428

Table 4.9
Validation Design Combinations

Design	S (mm)	W1 (mm)	W2 (mm)	W3 (mm)	ϵ_{rf}
17a	0.25	0.3745	0.166	0.125	400
19a	0.3745	0.3745	0.166	0.125	400
17b	0.25	0.3745	0.166	0.125	800
19b	0.3745	0.3745	0.166	0.125	800
17c	0.25	0.3745	0.166	0.125	1200
19c	0.3745	0.3745	0.166	0.125	1200

The simulated and modeled validation design output responses at the varied thin film relative permittivity of 400, 800 and 1200 were compared in the Tables 4.10 - 4.12.

Table 4.10
Output Response Comparison at $\varepsilon_{rf}=400$

File	Design 17		Design 19	
	Simulated	Modeled	Simulated	Modeled
Fr50	31.76	30.44	31.27	29.90
S11	-26	-14.88	-24	-15.06
BW	4.6	3.47	5	3.49
X50	-5.29	-20.92	-6.45	-20.02
Fr1	30.02	28.04	29.04	27.34
R1	83.13	135.60	90.22	138.84
Fr2	32.70	32.49	32.30	32.09
R2	38.45	27.95	38.15	29.47

Table 4.11
Output Response Comparison at $\varepsilon_{rf}=800$

File	Design 17		Design 19	
	Simulated	Model	Simulated	Model
Fr50	30.56	29.30	29.93	28.76
S11	-24	-12.92	-22	-13.10
BW	4.5	2.46	4.9	2.47
X50	-6.64	-26.23	-8.53	-26.22
Fr1	28.77	27.15	27.61	26.45
R1	84.78	148.22	94.85	151.46
Fr2	31.67	31.59	31.23	31.17
R2	36.05	23.77	35.52	25.29

Table 4.12
Output Response Comparison at $\varepsilon_{rf}=1200$

File	Design 17		Design 19	
	Simulated	Model	Simulated	Model
Fr50	29.39	28.28	28.68	27.74
S11	-22	-11.56	-19.5	-11.71
BW	4.3	1.13	4.7	1.34
X50	-8.35	-32.03	-10.83	-32.45
Fr1	27.52	26.21	26.31	27.51
R1	89.35	166.70	101.53	169.94
Fr2	30.69	30.74	30.24	30.34
R2	34.10	20.50	33.07	22.02

Note from the previous tables, that the values obtained from each model are close to the results obtained from the simulations. Therefore, it was proved that the models estimate well the output responses.

These models predicted very well the matching and dual resonant frequencies. The maximum error percentage for the matching resonant frequency was 4% and for the first and second resonant frequency it was 6% and 0.6% respectively. The minimum reflection model predicted results within a 42% error and the bandwidth model predicted within a 24% error. Although they did not predict results as well as the resonant frequency models they did estimate reflections less than -10 dB with good bandwidth, which did comply with the desired goals.

A noticeable difference was observed in the dual resonance resistance models. These models yielded results with 63% and 27% error for the first and second resonant input resistances. The difference that was encountered between the modeled and simulated values was due to the fact that the model was an equation that consisted only of the most significant input factors accompanied by their respective coefficients.

It was desired that this antenna be tunable, matched at 50 ohms, operational at Ka-band, with good reflections and high bandwidth. Therefore, the generated models did let us know if the input factors used gave good or bad output responses.

4.7 Film Characterization Scan

A θ - 2θ scan was performed on the BSTO/MgO sample by X-ray diffraction (XRD) to determine the orientation of the film with respect to the normal direction of the substrate. This plot presents the diffraction intensity for atomic planes parallel to the surface of the sample. The θ - 2θ scan was performed between 5° and 60° . Figure 4.16 shows the XRD 2-theta scans for BSTO films on MgO. The strong (100) and (200) peak (22.43° and 45.84°) of the BSTO layer show that it has a preferred crystal orientation with the (100) planes parallel to the surface. This plot confirms that the BSTO has a cubic like structure. The other intensities present were from the MgO substrate (43.26°) and other oxide combinations. These oxide combinations were possible due to relatively low temperature achieved for deposition.

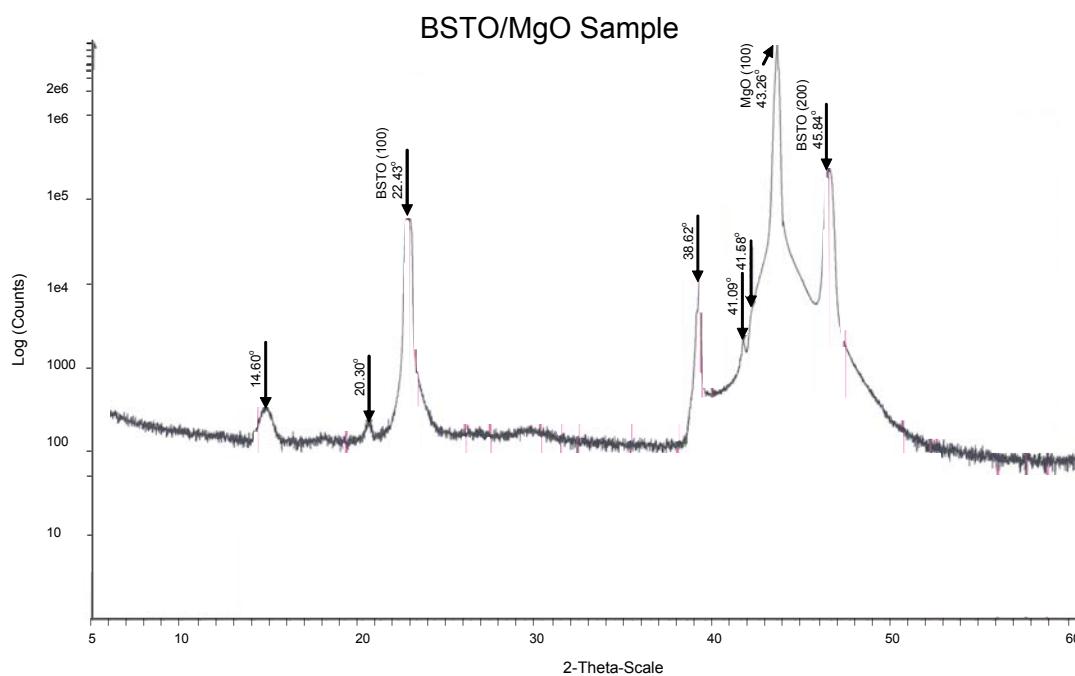


Figure 4.16. θ - 2θ scan of the BSTO/MgO sample.

The substrate was parallel to target at a separation distance of 4 cm. The target was rotated to make use of as

much as possible of the target area since the laser spot usually has the dimensions of a couple of millimeters. Due to error, the substrate was slightly displaced from the front of the target at the moment of placing the substrate in the deposition chamber. Therefore, the BSTO material grew more to the corner of the substrate which made it not suitable for antenna fabrication. It was not possible to deposit additional samples due to malfunction of the heater.

CHAPTER 5

Conclusions and Recommendations

5.1 Conclusions

The most important achievement of this thesis research was the design and characterization of a tunable coplanar waveguide (CPW) fed folded-slot antenna (FSA). This was possible due to the use of a thin film ferroelectric material (BSTO) grown by pulsed laser deposition (PLD) on a MgO substrate. The relative permittivity of this film varies with the application of an electric field. This variation in relative permittivity allowed the antenna to be tunable while operating at considerable input impedance, reflections, bandwidth and gain.

The antenna configuration developed to achieve the desired goals consisted of two layers: one was the MgO substrate, deposited on top of this layer was the BSTO ferroelectric material, and on the Au ground plane, the folded-slot antenna was fed by coplanar waveguide transmission lines. The antenna simulations were done in XFDTD from Remcom Inc. The number of simulations and antenna input parameter combinations were determined using a geometrical design obtained through the Design of Experiment (DoE) technique.

Bull's Eye plots were used to interpret the simulated output responses. The goal responses of wide bandwidth and matching resonant frequency at Ka-band with minimum reflections were observed in a tunable FSA with its top slot width ($W1$) at its high level dimension and its separation between the top and bottom slots (S) at its low level dimension with its side ($W2$) and bottom slot ($W3$) widths at

their low or high level dimension. The dual resonance behavior that occurred, as the thin film relative permittivity increased was a decrease of 1 GHz at the resonant frequencies, an increase of 20 ohms the first resonant input resistance and a decrease of 3 ohms at the second resonant input resistance.

Goal-models were generated with the output responses in order to study through equations the effect the input factors had on each output responses. These models predicted very well the matching and dual resonant frequencies. Their error percentage was 4% for the matching resonant frequency and 6% and 0.6% for the first and second resonant frequency respectively. The minimum reflection model predicted results within a 42% error and the bandwidth model predicted within a 24% error. Although these results were high they did estimate reflections less than -10 dB with good bandwidth, which did comply with the desired goals. The first and second resonant input resistance models yielded results with 63% and 27% error respectively. The difference that was encountered between the modeled and simulated values was due to the fact that the model was an equation that consisted only of the most significant input factors accompanied by their respective coefficients.

The optimum CPW-fed FSA dimensions such as $L/L1/S/W1/W2/W3 = 5.068/2.034/0.3125/0.437/0.166/0.125$ and feed dimensions of $Lf/Wf/Sf = 0.1875/0.083/0.2905$, all dimensions in mm, were obtained. The designed antenna was operational at Ka-band, matched at 50 ohms with good reflections ($S_{11} < -20$ dB), and tunable bandwidth of 7.10 GHz for 23.33% around 30.47 GHz. A total frequency shift of 4 GHz and input resistance shift of 28.54 ohms were obtained. The gain was approximately 2.98 dBi. The deposited BSTO material grew with a *c* crystal orientation perpendicular to the MgO substrate.

5.2 Recommendations

The CPW-fed FSA could be simulated in other programs or electromagnetic simulators, to analyze any discrepancies in the results. The antenna structure should be constructed and measurements taken in order to verify the antenna operation and compare the simulated results with the measured results. To facilitate the FSA fabrication the optimum antenna dimensions could be changed. The feed width dimension could be considered. This width could be wider to avoid that the ground plane material spills in this area during construction. Instead of fabricating the FSA through lift-off mask it could be constructed by other methods in order to avoid this spill of material.

The BSTO material should be studied by changing the substrate type, film thickness and composition in order to study its dielectric properties (relative permittivity, and dielectric loss) as a function of applied electric field. The thickness of the MgO and BSTO materials should be also characterized to predict the trend in the dielectric constant as a function of the misfit between the film and substrate. Also, other ferroelectric material such as Strontium Titanate Oxide, SrTiO_3 (STO) or other substrate materials such as Lanthanum Aluminate Oxide, LaAlO_3 (LAO) could be considered.

The BSTO films could be post-deposition annealed in flowing oxygen at high temperatures, from 900°C to 1350°C approximate, to improve their crystal quality. They could also be grown by sol-gel technique, which is a chemical method by liquid phase that enables dopants to be uniformly distributed throughout the entire BSTO ceramic.

References

- [1] Lopez-Rivera, N. and Rodríguez Solís, R., "Impedance Matching Technique for Microwave Folded Slot Antennas", Antennas and Propagation Society International Symposium, Vol. 3, 2002, pp. 450-453.
- [2] Li, K., Cheng, C.H., Matsui, T. and Izutsu, M., "Coplanar Patch Antennas: Principle, Simulation and Experiment", Antennas and Propagation Society International Symposium, Vol. 3, July 2001, pp. 402-405.
- [3] Neto, A., Maci, S. and de Maagt, P.J.I., "Slot Antennas Fed by Coplanar Waveguide", Antennas and Propagation Society International Symposium, Vol. 3, 2000, pp. 1588-1591.
- [4] Weller, T.M., Katehi, L.P.B. and Rebeiz, G.M., "Single and Double Folded-Slot Antennas on Semi-Infinite Substrates", IEEE Microwave Guided Wave Letter, Vol. 2, NO. 4, 1991, pp. 138-139.
- [5] Tsai, H-S and York, R.A., "FDTD Analysis of CPW-Fed Folded Slot and Multiple-Slot Antennas on Thin Substrates", IEEE Trans. Antennas Prop., Vol. 44, NO. 2, Feb 1996, pp. 217-225.
- [6] Tsai, H.S. and York, R.A., "Polarization-rotation quasi-optical reflection amplifier cell", IEE Electronics Wave Letters, Vol. 29, NO. 24, November 1993, pp. 2125-2127.
- [7] Matsuzawa, S. and Ito, K., "FDTD Analysis of Circularly Polarized Slot Array Antenna Fed by Coplanar Waveguide", Antennas and Propagation Society International Symposium, Vol. 2, July 1997, pp. 1264-1267.
- [8] Tsai, H.S., Rodwell, M.J.W. and York, R.A., "Planar Amplifier Array with Improved Bandwidth using Folded-Slots", IEEE Microwave Guided Wave Letters, Vol. 4, NO. 6, April 1994, pp. 112-114.
- [9] Luxey, C., Dussopt, L., Le Sonn, J-L and Lahourte, J-M, "Dual-Frequency Operation of CPW-fed Antenna Controlled by Pin Diodes", IEE Electronics Wave Letters, Vol. 36, NO. 1, January 2000, pp. 2-3.

- [10] Jose, K.A., Varadan, V.K. and Varadan, V.V., "Experimental Investigations on Electronically Tunable Microstrip Antennas", Microwave and Optical Technology Letters, Vol. 20, NO. 3, February 1999, pp 166-169.
- [11] Vinoy, K.J., Jose, K.A., Varadan, V.K. and Varadan, V.V., "Gain Enhanced Electronically Tunable Microstrip Patch Antenna", Submitted to Microwave and Optical Technology Letters, 2000.
- [12] Teo, P.T., Vinoy, K.J., Jose, K.A., Varadan, V.K. and Varadan, V.V., "Design and Development of Tunable Multi-Layer Smart Antennas using Ferroelectric Materials", Submitted to IEEE Trans. Antennas Prop, 2001.
- [13] Sheen, D.M., "Numerical Modeling of Microstrip Circuits and Antennas", Ph.D. Thesis, Department of Electrical Engineering and Computer Science at Massachusetts Institute of Technology, Jun 1991, pp 128-137.
- [14] Liang, G.C., Liu, Y.W. and Mei, K.K., "Full-wave Analysis of Coplanar Waveguide and Slotline using the Time-Domain Finite-Difference Method", IEEE Trans. Microwave Theory Tech., Vol. 37, Dec 1989, pp. 1949-1957.
- [15] Colom, J. G., Barton, R. R., Carpenter, L., and Rodriguez Solís, R., "A Novel Graphical Technique for Selection of a Robust Design Point", Proceedings of the 2001 American Society for Engineering Education Annual Conference & Exposition, 2001.
- [16] Hedblom, P., "Ferroelectric Thin Films by Pulsed Laser Deposition and Sol-gel Techniques: Processing and Characterization".
<http://web.kth.se/fakulteter/TFY/kmf/Hedblom.pdf>
- [17] Miranda, F.A., Subramanyam, G.S., Van Keuls, F.W., Romanofsky, R.R., Warner, J.D. and Mueller, C.H., "Design and Development of Ferroelectric Tunable Microwave Components for Ku- and K-Band Satellite Communication Systems", IEEE Trans. Antennas Prop., Vol. 43, No. 12, December 1995, pp. 1423-1428.